The Astronomical Journal, 131:2859–2876, 2006 June


# THE *SPITZER SPACE TELESCOPE* EXTRAGALACTIC FIRST LOOK SURVEY: 24 $\mu$m DATA REDUCTION, CATALOG, AND SOURCE IDENTIFICATION

Dario Fadda, Francine R. Marleau, Lisa J. Storrie-Lombardi, David Makovoz, David T. Frayer, P. N. Appleton, L. Armus, S. C. Chapman,[1] P. I. Choi, F. Fang, I. Heinrichsen, G. Helou, M. Im,[2] M. Lacy, D. L. Shupe, B. T. Soifer, G. K. Squires, J. Surace, H. I. Teplitz, G. Wilson, and L. Yan

*Spitzer* Science Center, California Institute of Technology, MC 220-6, Pasadena, CA 91125; fadda@ipac.caltech.edu

*Received 2005 December 30; accepted 2006 March 6*

## ABSTRACT

We present the reduction of the 24 $\mu$m data obtained during the first cosmological survey performed by the *Spitzer Space Telescope*. Images of a region of sky at moderately high Galactic latitude ($l = 88.^{\circ}3$, $b = +34.^{\circ}9$) were obtained on 2003 December 9–11. The survey consists of a shallow observation of $2.^{\circ}5 \times 2^{\circ}$ centered at $17^{h}18^{m}$, $+59^{\circ}30'$ (main survey) and a deeper observation of $1^{\circ} \times 0.^{\circ}5$ centered at $17^{h}17^{m}$, $+59^{\circ}45'$ (verification survey). Issues with the reduction of the 24 $\mu$m MIPS data are discussed and solutions to attenuate instrumental effects are proposed and applied to the data. Approximately 17,000 sources are extracted with a signal-to-noise ratio (S/N) greater than 5. The photometry of the point sources is evaluated through point-spread function (PSF) fitting using an empirical PSF derived from the data. Aperture corrections and the absolute calibration have been checked using stars in the field. Astrometric and photometric errors depend on the S/N of the source varying between $0.''35$–$1''$ and 5%–15%, respectively, for sources detected at 20–5 $\sigma$. The fluxes of the 123 extended sources have been estimated through aperture photometry. The extended sources cover less than 0.3% of the total area of the survey. Based on simulations, the main and verification surveys are 50% complete at 0.3 and 0.15 mJy, respectively. Counterparts have been searched for in optical and radio catalogs. More than 80% of the 24 $\mu$m sources have a reliable optical counterpart down to $R = 25.5$; 16% of the sources have a 20 cm counterpart down to 0.1 mJy and $\sim$80% of the radio-IR associations have a reliable optical counterpart. A residual map is obtained by subtracting point sources detected at the 3 $\sigma$ level and interpolating the regions occupied by extended sources. Several Galactic clouds with low and intermediate velocities are identified by comparison with neutral hydrogen data from this field.

*Key words:* catalogs — infrared: galaxies — surveys — techniques: photometric

*Online material:* machine-readable tables

## 1. INTRODUCTION

In 2003 December, during its first scientific campaign, the *Spitzer Space Telescope* (Werner et al. 2004) completed its first extragalactic survey in the far-IR. Almost 27 hr of observations with MIPS (Multiband Imaging Photometer for *Spitzer*; Rieke et al. 2004) were used to scan several times 5 deg$^2$ of sky in the direction $17^{h}18^{m}$, $+59^{\circ}30'$. The region was observed simultaneously in three different bands (24, 70, and 160 $\mu$m), thanks to the multiband capability of MIPS.

In this paper we present the reduction and analysis of the 24 $\mu$m data. Although the far-IR bands better sample the maxima of emission of the IR sources, the 24 $\mu$m band is the best band for extragalactic studies thanks to the high sensitivity of the 24 $\mu$m array and to the fair spatial resolution ($5.''9$ point-source function [PSF] FWHM) of the instrument. IRAC (Infrared Array Camera; Fazio et al. 2004) data were also obtained. These have been used to help in the identification of optical counterparts and to better define the spectral energy distribution (SED) of the detected sources (Lacy et al. 2005).

The improvement of depth and quality of the mid-IR images with *Spitzer* is huge with respect to previous space missions. *IRAS* (Soifer et al. 1983) surveyed the same region of sky at 25 $\mu$m and detected only six sources. Although the *Infrared Space Observatory* (*ISO*; Kessler et al. 1996) did not observe the First Look Survey (FLS) field, several surveys have been conducted at 15 $\mu$m. The most extended in the ELAIS-S1 and Lockman regions (Gruppioni et al. 2002; Fadda et al. 2004b) covered 2 and 0.55 deg$^2$, respectively. They reached a depth of 1 and 0.45 mJy detecting 100 and 480 sources per square degree (31 and 5 times less than the source density in the main field and 76 and 16 times less than the source density in the verification field), respectively. Only the deepest surveys (like the Hubble Deep Field–North [HDF-N]; Serjeant et al. 1997) reached a sensitivity comparable to that of the FLS but on an area 500 times smaller than that of the FLS verification field. Moreover, the different wavelength coverage makes possible the detection of galaxies up to a redshift of 2.5, a region inaccessible to the *ISO* 15 $\mu$m surveys.

This substantial leap in observational capabilities led to the execution of the FLS using director's discretionary time. The early release of data from this survey gave general observers real data to assist in planning of their Cycle 1 proposals rather than basing extragalactic observations on highly extrapolated models. A subset of the data was released in 2004 January, and the full pipeline-processed data set was released when the *Spitzer* archive opened (2004 May). This paper presents the state-of-the-art reduction based on tools developed at the *Spitzer* Science Center (SSC).

The main goals of the surveys were (1) to detect enough extragalactic sources at unexplored sensitivity levels in order to generate a representative sample and to reduce the uncertainties in source counts (see Marleau et al. 2004); (2) to characterize the

[1] Department of Astronomy, California Institute of Technology, MS 320-47, Pasadena, CA 91125.

[2] Astronomy Program, School of Earth and Environmental Sciences, Seoul National University, Shillim-dong, Kwanak-gu, Seoul 2-880-9010, South Korea.

TABLE 1
DESCRIPTION OF THE OBSERVATIONS

| AOR Key | Date of Start | Date of End | DCEs × Legs | Total Exposure Time[a] (s) |
|---|---|---|---|---|
| 3865856..... | 2003 Dec 9 16:56:13 | 2003 Dec 9 18:13:46 | 101 × 10 | 3696.2 |
| 3866112..... | 2003 Dec 9 18:22:45 | 2003 Dec 9 19:40:15 | 101 × 10 | 3696.2 |
| 3866368..... | 2003 Dec 9 20:28:46 | 2003 Dec 9 21:46:23 | 101 × 10 | 3696.2 |
| 3866624..... | 2003 Dec 9 21:55:22 | 2003 Dec 9 23:12:56 | 101 × 10 | 3696.2 |
| 3863808..... | 2003 Dec 9 13:38:51 | 2003 Dec 9 15:48:44 | 301 × 6 | 6621.7 |
| 3864064..... | 2003 Dec 10 06:54:29 | 2003 Dec 10 09:28:46 | 301 × 7 | 7725.3 |
| 3864320..... | 2003 Dec 10 15:44:45 | 2003 Dec 10 18:18:58 | 301 × 7 | 7725.3 |
| 3864576..... | 2003 Dec 10 23:50:42 | 2003 Dec 11 02:00:31 | 301 × 6 | 6621.7 |
| 3864832..... | 2003 Dec 10 04:14:42 | 2003 Dec 10 06:24:35 | 301 × 6 | 6621.7 |
| 3865088..... | 2003 Dec 10 12:39:49 | 2003 Dec 10 15:14:07 | 301 × 7 | 7725.3 |
| 3865344..... | 2003 Dec 10 18:49:38 | 2003 Dec 10 21:23:53 | 301 × 7 | 7725.3 |
| 3865600..... | 2003 Dec 11 02:30:34 | 2003 Dec 11 04:40:22 | 301 × 6 | *6618.0 |

[a] An asterisk indicates that one DCE was not transmitted.

dominant source populations with both MIPS and IRAC data from *Spitzer*, plus ancillary data at optical, near-IR, and radio wavelengths (see, e.g., Yan et al. 2004; Appleton et al. 2004), and (3) to explore the cirrus foreground at moderately high Galactic latitudes and its effect on point-source detectability.

The choice of FLS field was dictated by observational constraints. It corresponds to the region in the continuous viewing zone of the satellite with the lowest cirrus contamination (1.1 MJy sr$^{-1}$ at 100 $\mu$m; Schlegel et al. 1998). In this way, the FLS was observable in the first scientific campaign independent of the launch date. Since the field is a new cosmological field, a series of ancillary observations were obtained to support the *Spitzer* data. Deep optical data in the *R* band and Very Large Array (VLA) data at 20 cm are already publicly available (Fadda et al. 2004a; Condon et al. 2003). The field is part of the Sloan Digital Sky Survey (SDSS; D. W. Hogg et al. 2006, in preparation).[3] Moreover, the field has been observed in $i'$ and $g'$ with the 200 inch (5.1 m) Palomar LFC camera (T. M. Glassman et al. 2006, in preparation), in $u'$ and $g'$ with the Canada-France-Hawaii Telescope Megacam (Shim et al. 2006), and in $J$ and $K_s$ with Kitt Peak National Observatory (KPNO) FLAMINGOS (P. I. Choi et al. 2006, in preparation), and redshifts have been collected with the Wisconsin-Indiana-Yale-NOAO (WIYN) Hydra (Marleau et al. 2003) and Keck DEIMOS (Choi et al. 2005). Finally, to better study the impact of the cirrus emission on extragalactic surveys, an H I image of the field has been obtained with the Green Bank Telescope (Lockman & Condon 2005).

In this paper we discuss in detail the reduction of the data as obtained from the *Spitzer* archive, providing a catalog and identifications of the sources with optical and radio counterparts. Section 2 presents the observations and the set of data obtained. Section 3 describes the steps in the data reduction. The source extraction is discussed in § 4, which also includes a study of the photometric calibration based on stars detected in the FLS field (calibration factor and PSF estimation). The cirrus foreground is presented in § 5, and the main clouds are identified by comparison with the H I observations. Section 6 describes the identification of optical and radio counterparts. Finally, in § 7 images and catalogs are presented, and a summary is drawn in § 8.

## 2. OBSERVATIONS

The observations of the FLS field were carried out using 12 AORs (astronomical observation requests) in 3 days of the first MIPS scientific campaign (2003 December 9–11) in nominal operations. The *main* field ($2.^\circ5 \times 2^\circ$) was surveyed with eight AORs to obtain an average effective integration time of 84 s per sky pixel. Four AORs were used to survey the *verification* region ($1 \times 0.5$ deg$^2$) obtaining an effective integration time of 426 s per sky pixel.

Compared to other extragalactic MIPS surveys, the main FLS is close to the six SWIRE surveys (Lonsdale et al. 2003) in terms of sky coverage (5 deg$^2$ compared to 4.8–11 deg$^2$ of the SWIRE surveys) and sensitivity (1.4 times lower than that of the SWIRE surveys). The verification survey is similar to the guaranteed time observer (GTO) surveys (principal investigator [PI]: G. Rieke, in the Chandra Deep Field–South [CDF-S], SWIRE-XMM, HDF-N, and Lockman Hole fields), which cover between 0.4 and 0.67 deg$^2$ and are 1.4–2 times more sensitive. The Great Observatories Origins Deep Survey (GOODS; Dickinson 2001) covers an area 10 times smaller with a sensitivity 9 times better than that of the FLS verification survey.

As reported in Table 1, every AOR is a scan composed of a variable number of legs. During a scan leg, the motion of the satellite is compensated for by the movement of a mirror (called a cryogenic scan mirror [CSM]) that freezes the sky during the integration on the array. Fifty different positions of the CSM are used during each scan. Along a scan leg, a cycle of 25 different positions is repeated several times. Another set of 25 CSM positions is used to compensate for the satellite motion during the return scan leg. The AORs that cover the verification fields used a shorter scan leg than those in the main field and therefore have fewer exposures (or data collection events [DCEs]) per scan leg with respect to those in the main field.

IRAC observations (Lacy et al. 2005) covered approximately a square of $2 \times 2$ of the area observed with MIPS at 24 $\mu$m (see Fig. 1). MIPS observations at 70 and 160 $\mu$m (Frayer et al. 2006) cover approximately the same region observed at 24 $\mu$m since they were obtained at the same time. They are displaced by $12.''2$ and $7.''6$, respectively, with respect to the 24 $\mu$m image on opposite sides along the scan direction.

In Figure 1, locations of other public surveys performed in the area are shown. A wide-field KPNO survey in the *R* band (Fadda et al. 2004a) covers almost the entire area surveyed at 24 $\mu$m. The entire area has been also surveyed by the Sloan telescope in the five SDSS bands (D. W. Hogg et al. 2006, in preparation). Two radio surveys (20 cm with the VLA [Condon et al. 2003] and with the Westerbork [Morganti et al. 2004]) were done in preparation for the IR survey. Most radio sources with bright

[3] See http://ssc.spitzer.caltech.edu/fls/extragal/sdss.html.

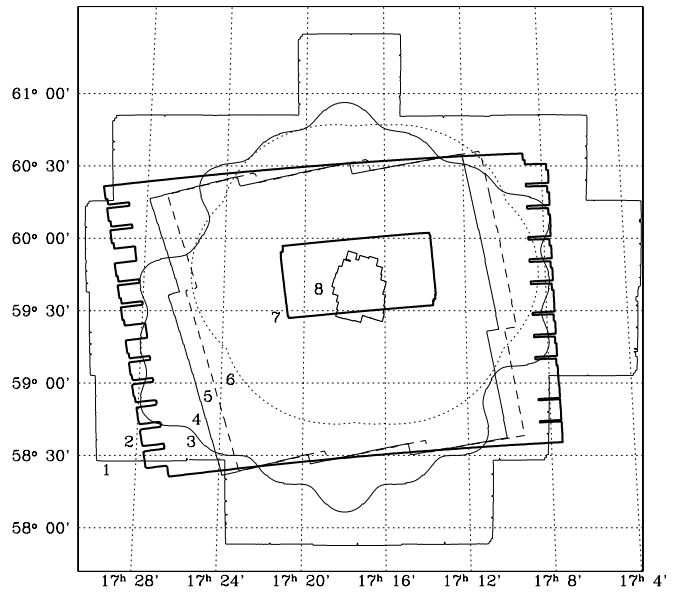


FIG. 1.—Coverage of public surveys in the FLS region. From the outside going toward the center: (1) KPNO *R* images (Fadda et al. 2004a), (2) 24 $\mu$m main field (this paper), (3) VLA 20 cm (Condon et al. 2003), (4) IRAC channels 1 and 3 (Lacy et al. 2005), (5) IRAC channels 2 and 4 (Lacy et al. 2005), (6) Westerbork Synthesis Radio Telescope (WSRT) 20 cm (Morganti et al. 2004), (7) 24 $\mu$m verification field (this paper), (8) *HST* ACS data (L. J. Storrie-Lombardi et al. 2006, in preparation). Regions similar to the 24 $\mu$m one have also been covered at 70 and 160 $\mu$m (Frayer et al. 2006).

optical counterparts ($R < 20$) have been spectroscopically followed-up with WIYN Hydra (Marleau et al. 2003). Virtually every radio source with a known redshift has a counterpart at 24 $\mu$m. Finally, a field of 0.12 deg$^2$ has been observed with the *Hubble Space Telescope* (ACS *I*-band parallel survey during NICMOS observations of extremely red objects [EROs]; L. Storrie-Lombardi et al. 2006, in preparation) in the region of deep 24 $\mu$m data (verification survey).

The passband of the MIPS24 filter is compared to the other *Spitzer* filters in Figure 2. It covers the wavelength range 20.7–25.8 $\mu$m (40% transmission limits), and its effective wavelength is 23.675 $\mu$m. Luminous IR galaxies ($L_{\rm IR} > 10^{11}\ L_\odot$) are common in high redshift surveys (see, e.g., Elbaz et al. 2002), and such galaxies can be seen in our survey up to a redshift of $\sim$2.5.

## 3. DATA REDUCTION

We started our data reduction with data obtained from the *Spitzer* science archive: basic calibrated data (BCDs) and flats computed for the MIPS campaign. For this paper we used the products from the SSC pipeline, version S10.5 (2004 May). The BCDs are individual frames already corrected for dark, flat, and geometric distortions. The darks used in S10.5 were computed from a set of observations obtained early in the mission, and the flats were obtained from scientific data of the entire MIPS campaign. For an optimized reduction we choose to improve the dark and flat corrections using the same set of data. This is possible since our observations are not dominated by background fluctuations. Therefore, once the sources are masked, the background is essentially flat.

### 3.1. *Dark Residuals and Jail Bars*

The 24 $\mu$m array has four independent output amplifiers servicing interleaved columns of arrays. This produces a characteristic dark-current pattern of four columns repeating across the array.

Residuals of a bad dark correction are visible in the archival flats. To correct for this effect, we deflattened the BCDs with the archival flats. These are a set of 50 images, each one corresponding to a different position of the CSM.

We median filtered every BCD with an $8 \times 8$ pixel box to obtain a smoothed background image and then subtracted from the original BCD. Then, masking every pixel affected by cosmic rays, we computed the median value of flux for the pixels corresponding to each one of the four amplifiers. The value obtained is the offset required to correct the dark applied to the BCD. In a second

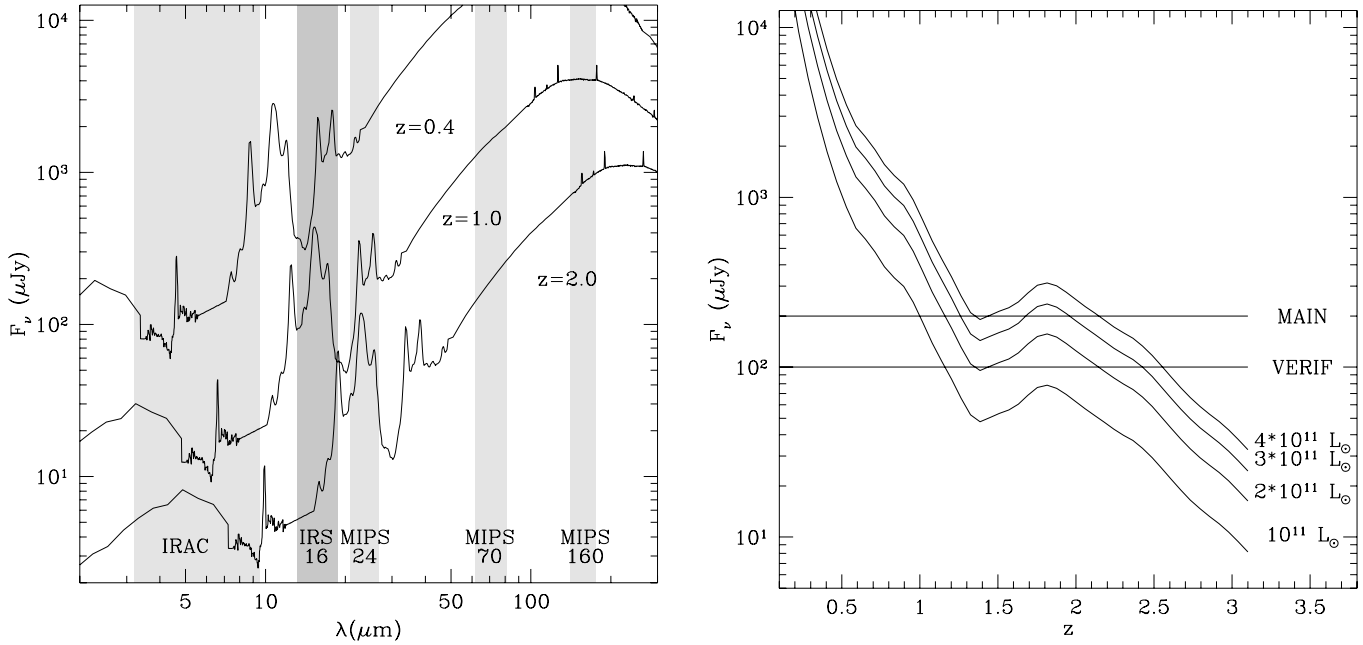


FIG. 2.—*Left:* Typical luminous IR galaxy ($L_{\rm IR} = 10^{11}\ L_\odot$) as seen at three different redshifts by different *Spitzer* detectors (SED of M82 renormalized). *Right:* The 24 $\mu$m flux of the same galaxy with different luminosities as a function of the redshift. Horizontal bars show the sensitivity limits of the main and verification survey. In the verification region, luminous IR galaxies can be detected up to a redshift of 2.5.

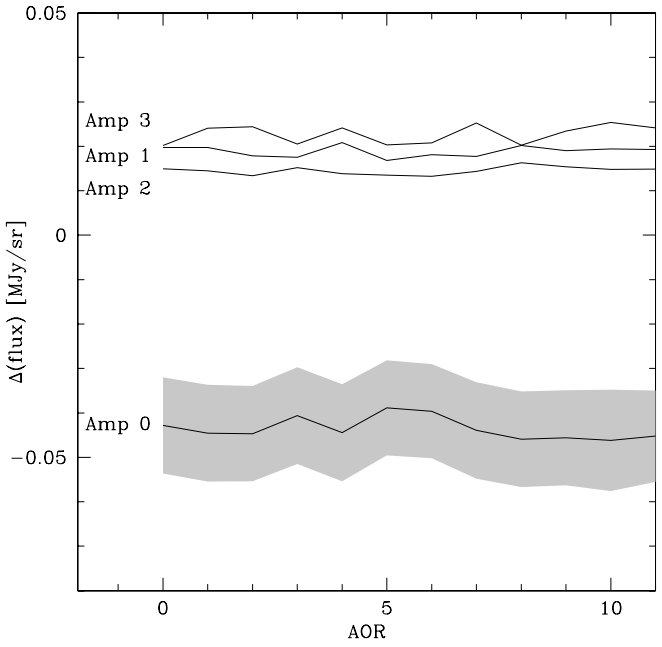


FIG. 3.—Median flux shift of pixels read by the four different amplifiers in the 24 $\mu$m array with respect to the smoothed image, as a function of the AOR. The median value for each AOR is shown. In the case of the first amplifier the error bar is also shown. Data have been corrected for this effect due to an imperfect dark subtraction.

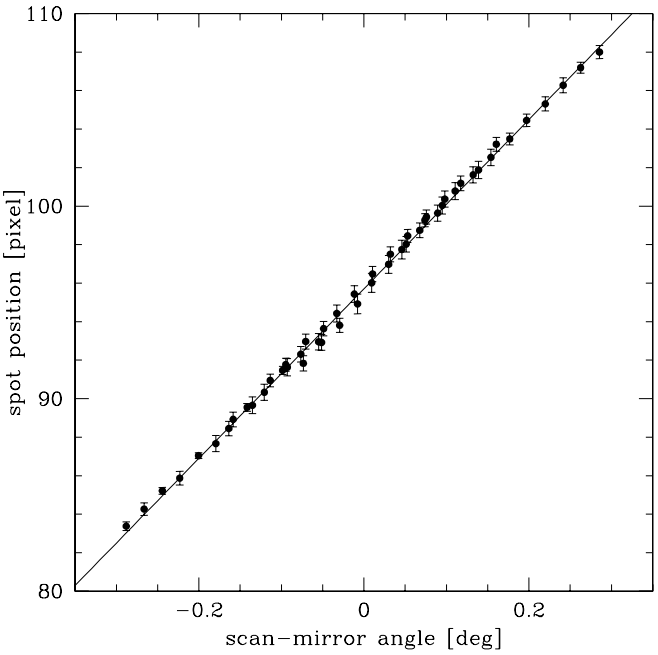


FIG. 4.—Scan mirror angle vs. $y$-pixel coordinate along column 116 of the biggest spot due to the pick-off mirror for the 50 different positions of the scan mirror used during the observations. The overplotted line is the fitted relationship, $y[\mathrm{pix}] = 95.7 + \mathrm{sm}[\,\mathrm{deg}\,]44.0$. The model used for computing the scan mirror position reproduces the actual position of the scan mirror very well.

iteration, when the first final map and a catalog of sources is obtained, sources are also masked.

As shown in Figure 3, the amplifier connected to the first column has a flux systematically lower than the other three. The difference is constant for every AOR, while very small variations occur among the different AORs. The amplitude of the difference (approximately 0.07 MJy sr$^{-1}$) corresponds to 1.5 times the noise in the final image; it is therefore a nonnegligible effect.

We computed the median value of the flux for every amplifier during each AOR and corrected the column flux of each BCD. After this additive correction, there are still a few BCDs that have dark latencies, especially after sudden variations in the incident flux, as after a reset of the detector or after a cosmic ray hit. In *Spitzer* jargon these are called "jail bars" because typically one out of every four columns is enhanced with respect to the others. Thus, a regular pattern of bars appear in the BCD, recalling the image of a prison window. An additive correction was applied to the BCDs, for which this effect is 5 times greater than the dispersion of the flux offsets.

In rare cases a few lines are enhanced in the array, probably because of a glitch in the electronics during the reading of the CCD. This effect is clearly visible in the HDF-N observations (see D. Fadda et al. 2006, in preparation). In the case of the present observations no BCDs were affected. Nevertheless, a few BCDs have a set of lines masked because of data transmission problems.

### 3.2. *CSM Effects on Flat and Illumination*

As previously discussed, the CSM is used to freeze the image of the sky during the integration since the observatory is continuously moving during the observations. Unfortunately, the pick-off mirror has some dirty spots that are projected on the array in different positions corresponding to the various CSM orientations. This means that flats have to be computed for each set of frames with the same CSM orientation. Moreover, since CSM positions vary slightly from AOR to AOR, and since latencies of bright objects from previous observations can be visible along an entire AOR, it is advisable to compute a different set of flats for each AOR. Since the FLS observations have very long AORs, there are enough frames to compute flats per each CSM position and per each AOR (36 and 20 in the main and verification surveys, respectively).

The position of the scan mirror at the beginning of each exposure found in the header of the BCDs is computed through a model. Since at least one spot is clearly visible in each frame, we have computed its position and compared it to the value in the header of the BCD to check the accuracy of the model predictions. In particular, we have considered the spot always present along column 116 of the array for the 50 positions of the CSM used during one AOR. To compute its position along the column we masked all the pixels affected by cosmic ray hits and/or sources and fitted a parabola. The minimum of the parabola fit gives the position of the spot. As visible in Figure 4, the position of the CSM computed with the model reproduces the actual position of the CSM very well.

A variation of the array illumination that correlates with the CSM orientation is also clearly visible in the history of the median fluxes (see Fig. 5). To better study this effect, we have considered the median fluxes of frames with the same CSM position and matched them to the CSM angles (Fig. 6). In detail, for all the frames with the same CSM position we have computed the median flux on the frame, subtracted the median flux of the entire observation, and computed the average and dispersion of the obtained values. The best match of the deviation from the median flux with the CSM angle is obtained by scaling the CSM angle by the factor 11.8. The correlation of the CSM positions with the illumination variation is striking except for the last CSM position. We applied a multiplicative correction to the data, since we noticed in the observations of standard calibrators that the flux of the stars in the different frames varied with the CSM angle in the same way as the background flux.

To correct for this effect we therefore used the CSM position (rescaled by the factor 11.8) for all the orientations but the last

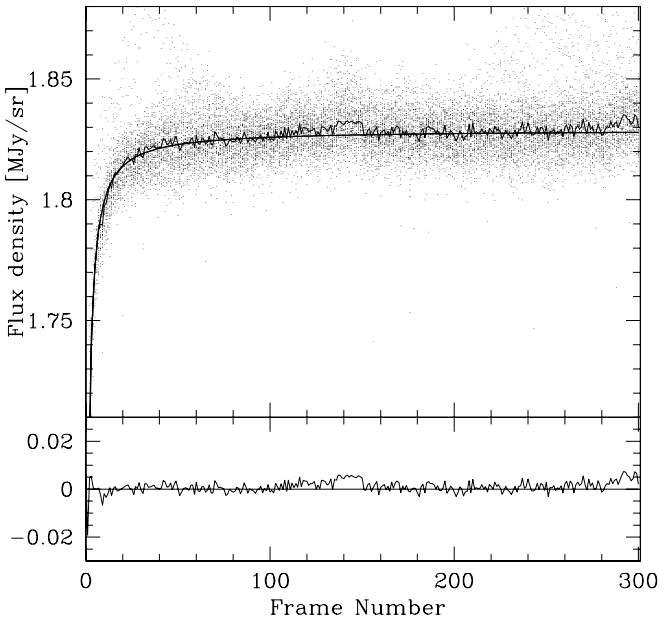


FIG. 5.—Long-term drift in the median flux as a function of the exposure number. A median transient (*thin line*) is computed by considering all the scan legs of the main survey (*circles*). An exponential function fitting the median behavior is used for the correction (*thick line*). The bottom part of the figure displays the residuals after applying the correction to the median line.

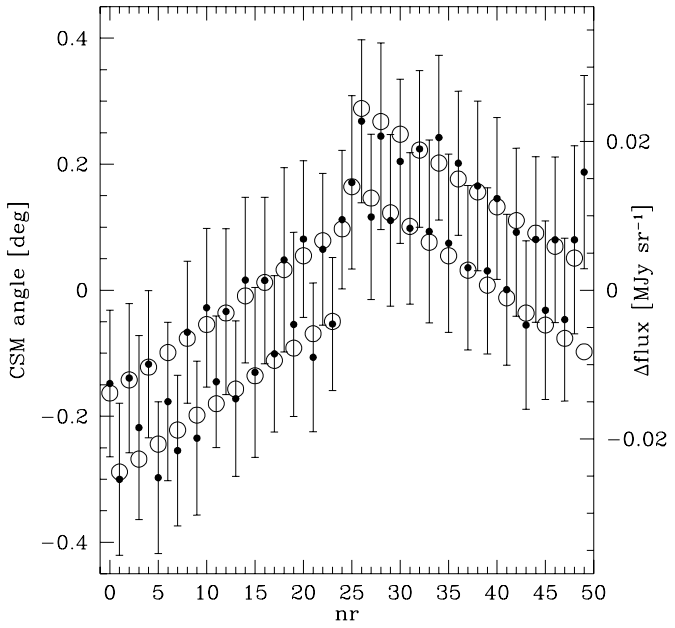


FIG. 6.—Average positions of the scan mirror during an integration (*open circles*) compared to the difference between the frame median flux and the median flux along the entire scan ( *filled circles with error bars*) for the 50 different positions of the scan mirror used during the observations. The first 25 positions are used during a fourth scan leg, the second 25 during a back scan leg. The flux differences have been matched to the scan-mirror angles by multiplying them by 11.8. The obtained match is very good, except for the last position, where the illumination is uncorrelated to the position of the scan mirror.

angle, for which we accepted the value from the actual measurement. It is not clear why the correlation fails for this CSM orientation. Since the CSM position is correctly modeled, as we can see from measuring the spot position on the array (see Fig. 4), the effect has to be related to another phenomenon. Moreover, in other medium-scan surveys recently reduced by the first author, the correlation works perfectly for all the positions of the CSM.

### 3.3. *Zodiacal Light and Long-Term Transients*

After correcting BCD median levels for the CSM-dependent illumination, there are still three other components that affect their median fluxes: zodiacal light, a long-term transient, and Galactic cloud diffuse emission. We have subtracted the variation due to the zodiacal light by using the Kelsall et al. (1998) model available through the Spot software used for planning *Spitzer* observations. In particular, we have computed the predicted value of the zodiacal light for every BCD, taking into account its sky position and the time of the observation. In this way we are able to model accurately the variations in the flux along the AORs, as shown in Figure 5, although the absolute flux obtained is probably incorrect.

Since we are interested not only in studying point sources in the field but also in retrieving the variations of the foreground due to Galactic cloud emission, we tried to model the long-term variation of the detector. This feature has been already detected with ISOCAM, and in that case an attempt at a correction was made using the redundancy of the observations (Miville-Deschênes et al. 2000).

In the FLS we have the advantage of having several AORs performed in exactly the same way in a region of sky with low Galactic IR foreground. We are therefore able to study the median behavior of the long-term transient by considering all the scan legs of each AOR, since at the beginning of each scan leg the detector is reset. Since the scan legs are each done in a different region of sky and the legs cover over $2^\circ$, the median behavior is independent of the small-scale variations due to Galactic cloud emission (the typical size of a cloud is less than half a degree). In Figure 7 all the BCD median fluxes are shown together after shifting each scan leg in flux to better match, in the sense of the minimum $\chi^2$, the scan leg with fewer variations (i.e., less foreground Galactic emission). An exponential function has been fitted to the points, and then the matching of the different scan legs has been repeated by shifting in flux the scan legs to match the fitted curve and refitting the function. The median behavior is well fitted by the exponential function

$$F(t) = 28.2e^{-0.04/t} - 26.37, \quad (1)$$

with time in seconds (time elapsed from the first exposure) and flux units in MJy sr$^{-1}$. The flux level computed with this function is then subtracted from each BCD to obtain a final mosaic with a median zero level conserving at the same time the structure of the Galactic foreground.

In the case of the verification survey, for which the scan legs are shorter, we have shifted all the scan leg BCD fluxes to match the function fitted with the main survey data. The shifts added to the function values have been subtracted from the BCDs.

The effects of CSM illumination correction, subtraction of zodiacal light, and long-term transients are shown in Figure 7 on the median BCD fluxes of a piece of an AOR. All these corrections are needed to match the backgrounds measured by different BCDs in the same region of the sky. If the BCDs are co-added without applying these corrections, the variations in the background increase the noise in the final image. As we see in § 5, we can in this way also recover the structure of the Galactic clouds emitting at 24 $\mu$m.

### 3.4. *Relative Offsets*

Although the pointing of *Spitzer* is very accurate, errors of the order of an arcsecond in the absolute pointing are expected. On

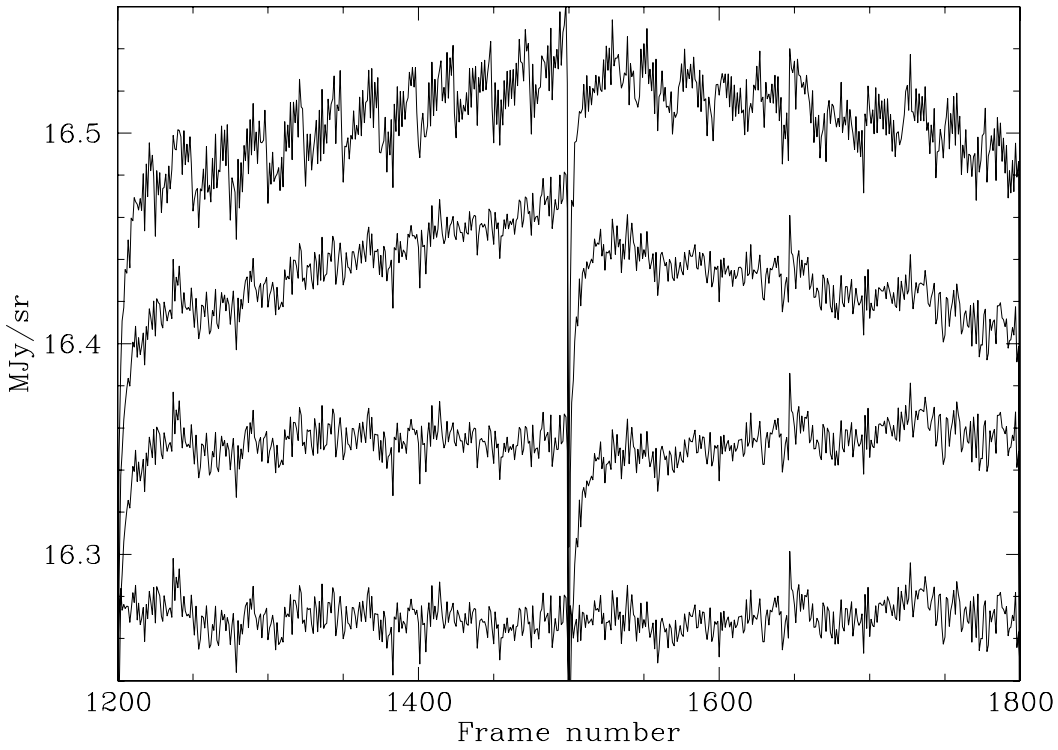


FIG. 7.—Effect of corrections on the median value of the frames of two main-survey subsequent scan legs. From top to bottom: the original median values of the frames; after scan-mirror illumination correction; after subtracting zodiacal light; after subtracting the long-term transient. The flux density refers to the uncorrected signal. The others have been arbitrarily shifted along the $y$-axis to show the effect of the corrections.

top of that, relative offsets are expected during an observation because the telescope is adjusting its pointing every time it moves. The biggest errors are therefore expected along the scan direction. If not corrected, these relative offsets affect the PSF in the final mosaicked image.

The ideal way to proceed would be to compute the offsets with respect to an image with accurate astrometry for each BCD. Unfortunately, the number of sources visible in each BCD is usually not high enough to compute an offset with a reasonable error. We therefore decided to co-add every 25 consecutive BCDs that have been observed by moving only the CSM. We expect in fact that the biggest errors in pointing occur when the telescope itself has moved.

As a reference image we used the SDSS $r'$ image of the field. This observation has the advantage of having accurate astrometry (error $<0\farcs1$) covering the entire field and to be sufficiently deep to find a high number of optical counterparts of the IR sources in every small mosaic. Typically, we find 50 sources with optical counterparts in each mosaic. The offsets are computed along and perpendicular to the scan direction. Figure 8 reports the number of sources used to compute the offsets and the offsets along the in- and cross-scan directions for every set of 25 BCDs. The shadows on the figure separate the different AORs. Considering the offsets in the in-scan direction, the offsets clearly depend on the direction of the scan leg. To achieve a better accuracy, one could in principle apply only two corrections per AOR along the in-scan direction corresponding to the two directions of the scan. We chose not to follow such a procedure because, in some cases, groups of images show a big deviation from this median behavior. Since, as shown in the bottom panel of Figure 8, the offsets are measured using around 50 sources, it is difficult to believe that these deviant offsets are simply due to insufficient statistics. The overall offsets along the two directions are always less than $1''$. The astrometry of each BCD has been updated according to the offsets measured in the two directions.

### 3.5. *Mosaicking*

A total of 19,691 BCDs were obtained in the FLS main and verification surveys; 92 of them have a shorter integration time and were obtained at the beginning of each scan leg. Although these frames can in principle be used, the detector is far from stabilization during these exposures, and typically they are affected by strong jail bars. We do not include these frames in our final image mosaics.

To co-add in a single map the remaining 19,599 BCDs we used MOPEX, a multipurpose tool developed at the SSC by D. Makovoz (see Makovoz & Marleau 2005) to find bad pixels, co-add, and extract sources. The final map has a pixel size of $1\farcs275$, half of the original pixel size. This allows us to exploit the superresolution due to the different observations taken with shifts of fractional pixels.

Although the SSC pipeline provides a mask of bad pixels that are damaged or saturated, several other pixels have to be masked because of cosmic rays. Among the several possibilities offered by MOPEX to detect these pixels, we choose the most conservative one that relies on redundancy.

As visible in Figure 9, the typical coverage is 22.6 and 114.4 in the main and verification surveys, respectively. This gives enough values to reject, with MOPEX, deviant pixels affected by cosmic rays. The rejection has been done in a conservative way using a top threshold of 5 $\sigma$ and a bottom threshold of 3 $\sigma$. Using too low a top threshold is dangerous, because this can mask the brightest pixels of bright objects, which usually have larger variance, or the faint wings of the PSF that are at the noise level.

Once the new masks are produced, a mosaic and a list of sources can be obtained. In order to improve our reduction, we

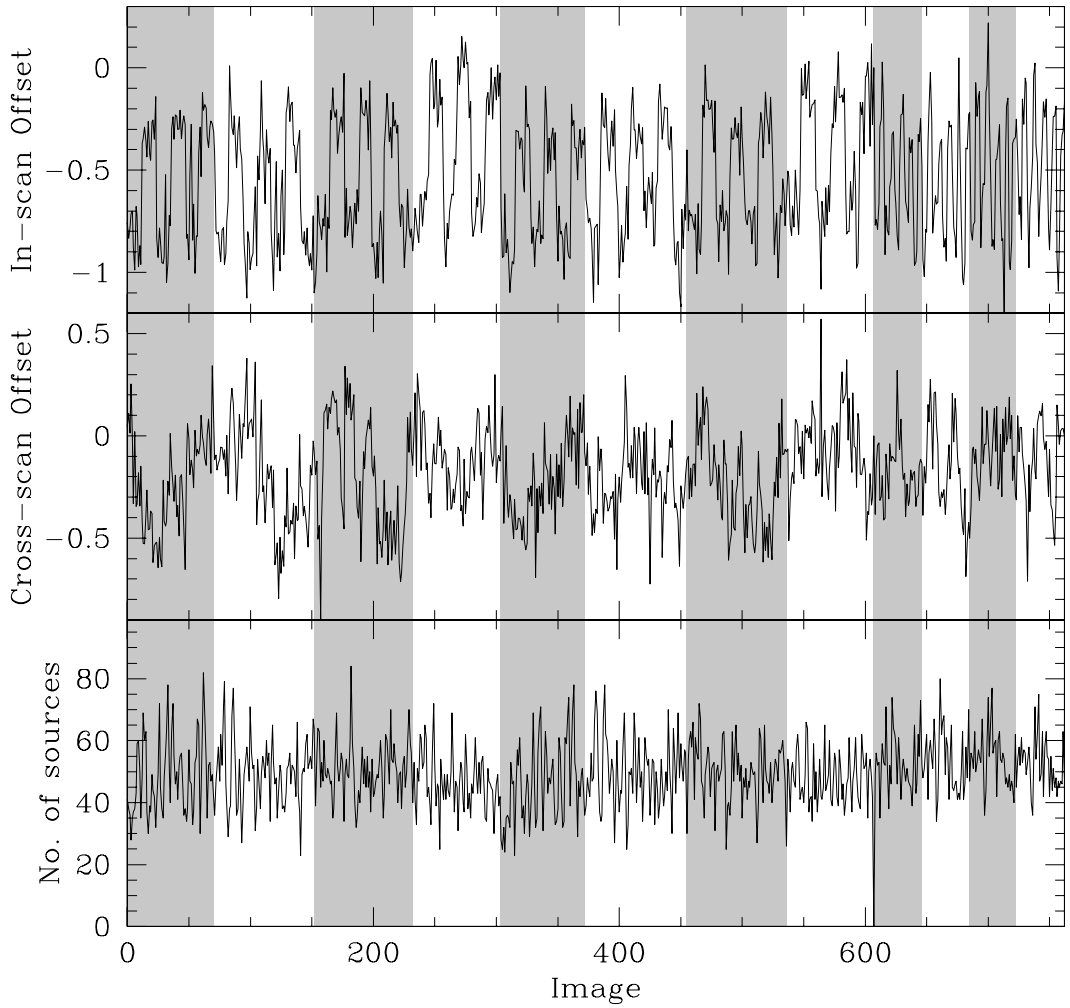


FIG. 8.—Offsets of groups of 25 images with the same telescope pointing along the in-scan and cross-scan directions in arcseconds, with respect to the $r'$ image of the field obtained by the SDSS. The bottom panel reports the number of sources with optical counterparts in each image used for computing the offsets. The gray and white background separates the different AORs.

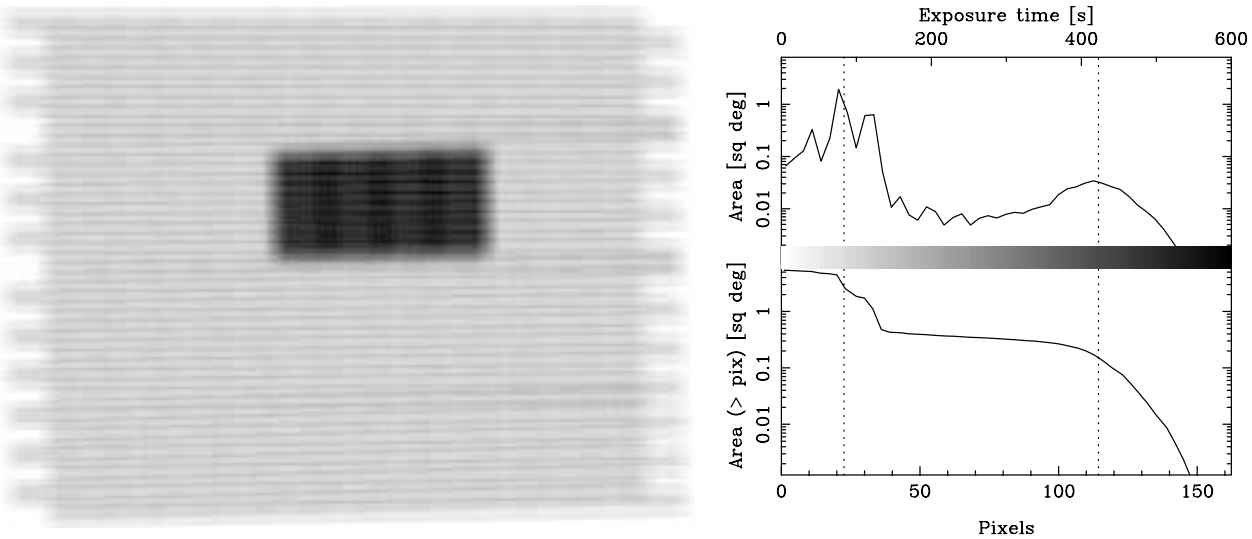


FIG. 9.—*Left:* Coverage map of the MIPS24 observations. *Right:* Differential (*top*) and cumulative (*bottom*) plots of the coverage vs. area. The two vertical dotted lines mark the median coverage in the main and verification surveys.

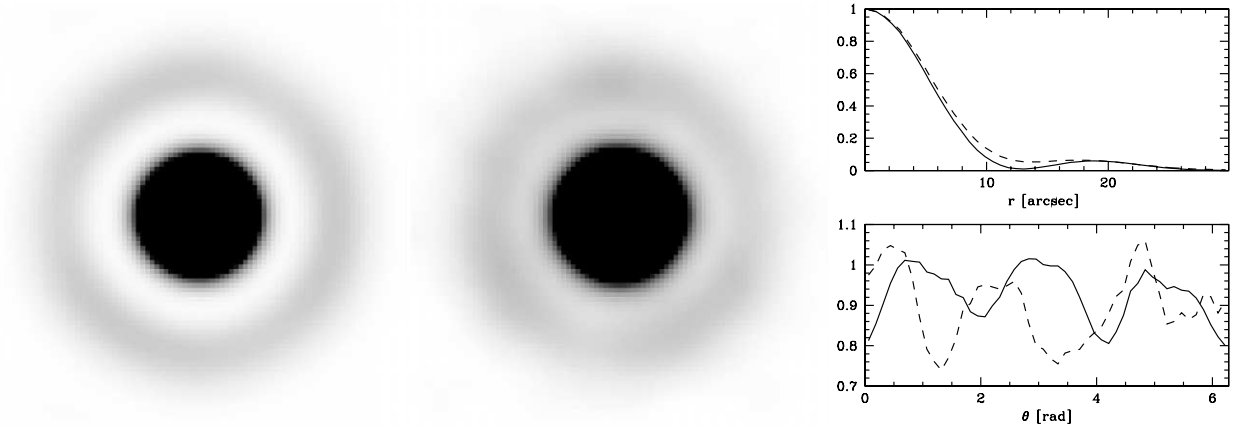


FIG. 10.— Theoretical (*left*) and empirical (*middle*) PRF evaluated by stacking 27 bright isolated point sources. On the right are the averaged radial profile (*top*) and averaged angular profile of the first Airy ring (*bottom*) for the two PRFs. The radial profiles are normalized with respect to their maxima, while the angular profiles are normalized with respect to their median values. Solid and dashed lines refer to the theoretical and empirical PRFs, respectively. The empirical PRF looks blurred with respect to the theoretical one and has a different angular profile.

used the improved masks and the list of sources to redo darks, flats, and further corrections based on the median flux of the BCDs by masking sources and bad pixels.

In cases of bright sources, latencies are visible in the BCDs taken after the observation of the bright source. In the case of our field, only one source is bright enough to produce latencies and therefore ghost sources in the final mosaic if these are not corrected. We corrected this case empirically as explained in § 4.5. We then reprojected the corrected BCDs to obtain a final mosaic. The namelist used for the projection is available through the SSC science archive (see § 7).

## 4. DATA ANALYSIS

### 4.1. *Source Extraction*

The point-source extraction was performed using the MOPEX software (Makovoz & Marleau 2005). The extraction was done in single-frame mode, i.e., using the same image for detection and fitting of point sources. The procedure used consists of the following steps.

In the first step, a sample of isolated and bright point sources was selected to estimate the empirical point response function (PRF) from the mosaic. The module *apex_1frame.pl* was run using a theoretical PRF produced by the STinyTim, the *Spitzer* version of the Tiny Tim PSF modeling program.[4] The mosaic is filtered with the simulated PRF to produce a point-source probability (PSP) image that is then used for detection. This filtering process enhances the point sources that match the input PRF while smoothing out noise features. The fitting was done without active deblending, and only the brightest isolated sources (flux $>5\times10^3$ $\mu$Jy) with the lowest $\chi^2$ ($\chi^2$/dof $< 30$) are kept. A total of 27 sources were selected for the PRF estimation.

The PRF was estimated in the second step using the module *prf_estimate.pl*. In our case, we selected a postage stamp size of $35\times35$ pixels and a radius of 11 pixels, which contains the first Airy ring. The PRF flux is normalized within that radius, and therefore, an aperture correction needs to be applied to the estimated fluxes (see § 4.5). Theoretical and empirical PRFs are shown in Figure 10. The PRF estimated from the data appears blurred with respect to the theoretical PRF. The different angular profile is due to differences between the model and the actual telescope, while the blurring is due to pointing uncertainties and sampling. The observed radial profile can be recovered by taking into account how the image is constructed, as done in the study of aperture corrections (see § 4.5). The angular structure depends on the details of the optics.

The first bright Airy ring around bright point sources causes many false detections in the mosaic image at faint flux levels. Therefore, our third step was to create a mosaic image for which all the point sources with S/N > 20 in the point source probability image have had their Airy rings removed. Using *apex_1frame.pl* with the empirical PRF, a second extraction at S/N > 20 was made obtaining a total of 1266 sources. A residual image was created using the module *apex_qa.pl* using a modified PRF with the region inside the first minimum set to zero.

The detection was then done on the ringless image with a much lower detection threshold. A total of 98,779 sources were detected. Finally, the fitting was done with passive and active deblending on the original mosaic using the list of sources detected on the ringless image. A total of 42,555 sources ($\sim1.0\times10^4$ sources deg$^{-2}$) with S/N > 3 were extracted. In the final catalog, we considered only sources with S/N > 5 in order to have a highly reliable list of sources. The module *apex_qa.pl* was used again to obtain an image without point sources to better estimate the flux of extended sources and to identify the emission from molecular clouds (see following sections).

### 4.2. *Extended Sources*

A few extended nearby objects are present in the observed field (see Fig. 11). These are resolved by MIPS at 24 $\mu$m, and we can therefore not extract them in the same way as the point sources. Most of the extended sources were identified by running the MOPEX module *run_bright_detect* and selecting sources with S/N > 20 and ellipticity >0.1. A total of 58 extended sources were identified in this way. To find other possible extended sources still undetected with the previous technique, we compared the flux in the central pixel with the flux inside a radius of 5″ as in Figure 12. If the source is extended, the flux is less concentrated than that of point sources so that the expected ratio between aperture and peak flux is higher than that of point sources. We did not consider in this search all the sources with companions within a radius of 8″, since the aperture flux is affected by the companion source. Usually, sources within this

[4] Developed for the *Spitzer* Science Center by J. Krist.

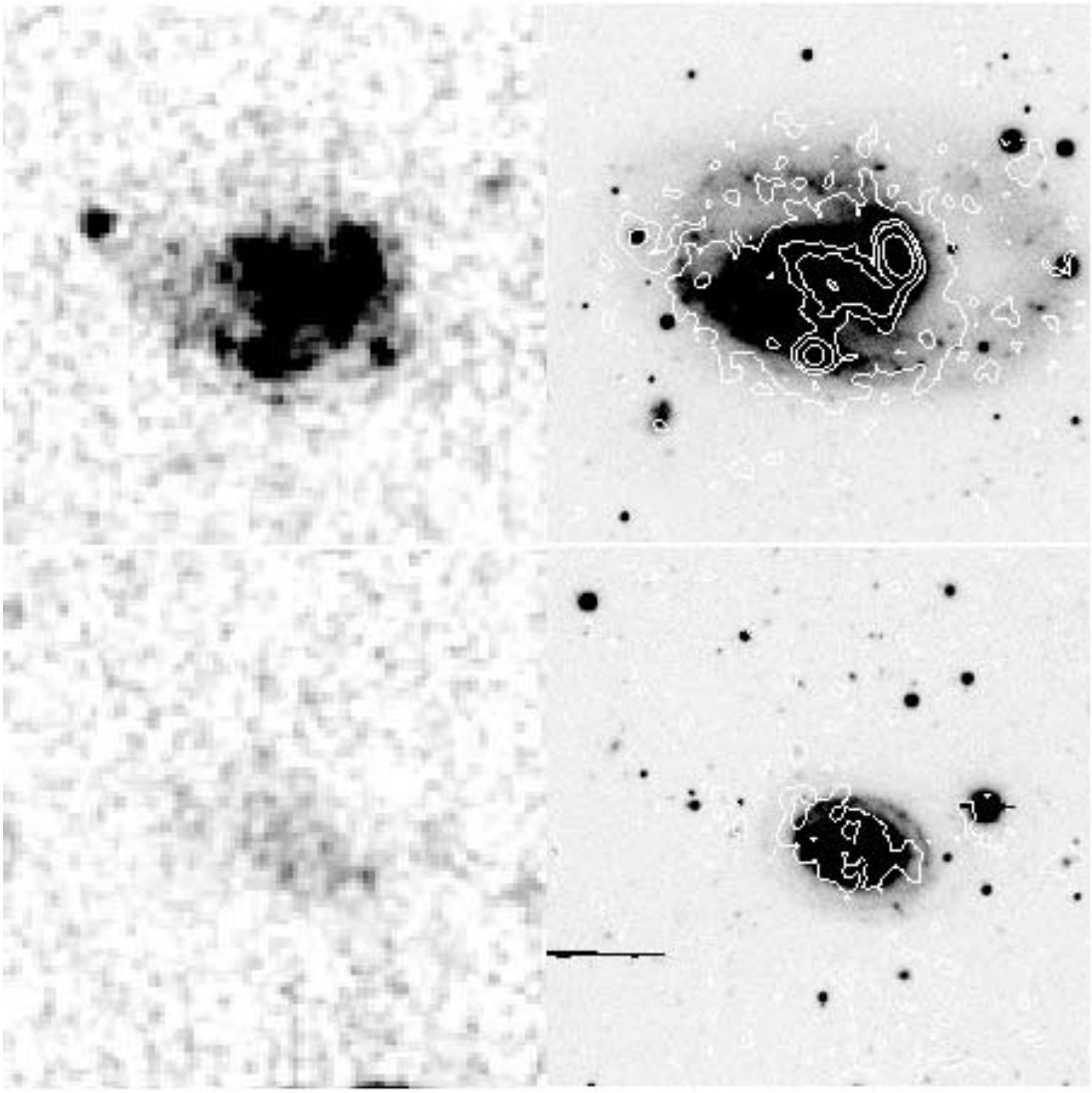

FIG. 11.—Two examples of extended 24 $\mu$m sources: the 24 $\mu$m image (*left*) and the *R* image (*right*) with isocontours at the 0.1, 0.3, 0.5, and 1 MJy sr$^{-1}$ levels. The images have a size of $2 \times 2$ and show a bright galaxy with several bright knots on the top and a low surface brightness galaxy at 24 $\mu$m on the bottom. The bright galaxy has been identified with the *run_bright_detect* module, while the second one was identified with the flux ratio diagram.

distance have been deblended by the extraction algorithm used or have been already identified as extended sources with the *run_bright_detect* module. We inspected visually the optical counterpart of each of the extended source candidates with ratio higher than the 3 $\sigma$ error band; 63 of them belong to extended objects. Most of the others are either undeblended objects or low-S/N sources with very uncertain fluxes. Two negative outliers were found at the border of the image, since the aperture used for computing the flux misses part of their flux. All the sources of the point-source catalog, falling on extended sources were then removed from the point-source catalog and a new residual image was obtained. The value of the total flux was determined by doing aperture photometry on the residual image with apertures large enough to contain the whole sources. The same apertures were masked to obtain a bad pixel list for the residual image, and the masked regions were interpolated. These regions cover a total area of less than 0.015 deg$^2$, i.e., 0.27% of the total area of the survey. The photometry of the brightest star in the field has also been evaluated inside an aperture. Although technically this is a point source, the PRF that we used was not large enough to do a correct fit, and we evaluated the total flux using aperture photometry. The first 10 entries of the extended sources list are given in Table 2. The table also reports the 20 cm flux of the VLA counterpart and the *R* magnitude of the optical counterpart. Redshifts measured by SDSS are also reported, if available.

### 4.3. *Completeness and Reliability*

To estimate the completeness and reliability of our point-source catalogs we performed simulations reinserting the extracted sources into the residual image. In particular, we divided the image into two regions according to the coverage: (1) coverage greater than 37 images (roughly corresponding to the verification survey; see Fig. 9) and (2) coverage between 10 and 37 images (the main survey except the noisy borders). Sources extracted (at the 3 $\sigma$ level) in one of these regions were reinserted in the same region at random positions using the empirical PRF estimated for the extraction with the module *apex_qa.pl*. The regions occupied by extended sources have been avoided.

In this way, no assumptions about counts and noise structure were made. Because of the imperfect subtraction of the sources, the noise is slightly higher than in the real case. The extraction of

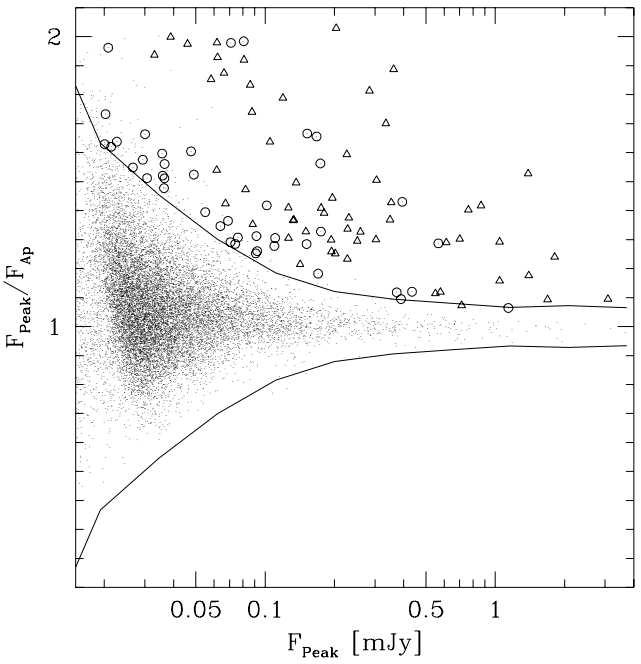


FIG. 12.—Ratio between peak and 5″ aperture fluxes. Points higher than the 3 $\sigma$ error band are candidate extended sources. The triangles represent the extended sources found with the *run_bright_detect* module. The points encircled appear extended in the optical images. The two negative outliers correspond to two sources on the border for which the aperture misses part of the flux.

the simulated sources was done in the same way as in the case of the real image. Inserted and extracted sources have been matched considering a maximum distance of 5″ and a difference in flux of 30%. The constraint in the flux helps in rejecting cases in which a source has been incorrectly deblended.

For completeness and reliability, we considered only sources detected with S/N > 5, since this is the limit chosen for our catalog in order to have a high reliability. As visible in Figure 13, the reliability is higher than 85% to the flux limits of our catalog (0.21 and 0.12 mJy for the main and verification surveys, respectively). At the 50% completeness limits, 0.3 and 0.15 mJy in the main and verification regions, respectively, the reliability is around 90%.

Finally, since some sources in our image could be transient sources, typically asteroids, we obtained two mosaics using images taken at different times (two consecutive legs of each scan) and subtracted one from the other to search for residual objects. No objects were found at the 5 $\sigma$ level.

### 4.4. *Photometric and Astrometric Accuracy*

Photometric and positional accuracies are assessed using the same simulations performed to estimate completeness and reliability. The photometric errors come from uncertainties in the extraction and in the flux calibration.

The uncertainty in the flux calibration is less than 5% (C. Engelbracht et al. 2006, in preparation). To evaluate the uncertainty in the extraction, we considered a plot of the difference between the true and measured flux normalized to the true flux versus the S/N of each detected source (see Fig. 14). The big circle in every S/N bin corresponds to the median value of the detected points. Since low S/N sources tend to be detected if they are on top of positive fluctuations of the noise, this effect creates a bias in the median estimated flux below S/N = 10. In our simulations this effect is enhanced because of the presence of residuals due to the imperfect subtraction of the real sources. Since this effect can be corrected only statistically, we did not apply any correction to the fluxes of the single sources. The 1 $\sigma$ error band is also shown on the plot (comprising the region between the 16th and 84th percentiles). The error increases from 5% at S/N = 20 up to around 15% at low S/N values. The errors reported in the catalogs are computed according to this curve.

Errors in the astrometry of the 24 $\mu$m sources come from the measurement on the image and from the pointing uncertainty. We evaluated the errors made in the extraction process through our simulations. As shown in Figure 15, this error depends on the S/N of the source. It is typically around 0.″8 for sources with S/N < 7 and becomes negligible beyond S/N = 20. In the case of bright sources, in fact, more pixels are seeing the source, and this improves the estimate of the center of the PSF. As explained in § 3.4, we corrected the astrometry of the BCDs taking as a reference the SDSS image of the field. Thanks to this, we do not have any relative offsets between the positions of our sources and their optical counterparts (see Fig. 16). The pointing error can be computed from the dispersion in the matching between IR sources and optical counterparts during the offset correction. This is around 0.″3. As visible in Figure 16 (*right*), the error computed by matching sources with their optical counterparts is asymptotically converging to this uncertainty. Considering that the optical uncertainty is around 0.″1, the error in the matching with the optical

TABLE 2
EXTENDED SOURCES

| Name (IAU) | R.A. (J2000.0) | Decl. (J2000.0) | Flux (24 $\mu$m) (mJy) | Flux (20 cm)[a] (mJy) | $R$ (mag) | $z$ | Notes |
|---|---|---|---|---|---|---|---|
| J170850.7+601144 | 17 08 50.744 | +60 11 44.11 | 7.44 | 1.119 | 15.13 | 0.0667 | |
| J170855.9+601114 | 17 08 55.957 | +60 11 14.93 | 59.04 | 2.230 | 15.49 | ... | |
| J171119.6+602619 | 17 11 19.621 | +60 26 19.20 | 4.29 | 0.530 | 15.96 | 0.0741 | |
| J171140.1+595944 | 17 11 40.194 | +59 59 44.79 | 31.56 | 0.435 | 13.61 | 0.0167 | |
| J171226.0+603024 | 17 12 26.040 | +60 30 24.69 | 3.55 | 1.283 | 15.86 | 0.1070 | |
| J171247.7+592705 | 17 12 47.736 | +59 27 05.19 | 4.18 | 0.565 | 16.46 | 0.1372 | |
| J171239.4+584147 | 17 12 39.482 | +58 41 47.18 | 9.01 | 0.940 | 17.50 | 0.1653 | |
| J171336.0+603006 | 17 13 36.010 | +60 30 06.47 | 5.39 | 0.231 | 20.77 | ... | |
| J171306.9+591923 | 17 13 06.903 | +59 19 23.55 | 8.82 | 0.532 | 15.07 | ... | |
| J171359.5+592017 | 17 13 59.529 | +59 20 17.03 | 4.00 | ... | 15.58 | 0.0544 | |

NOTES.—Units of right ascension are hours, minutes, and seconds, and units of declination are degrees, arcminutes, and arcseconds. Table 2 is published in its entirety in the electronic edition of the *Astronomical Journal*. A portion is shown here for guidance regarding its form and content.

[a] OOI stands for "out of image."

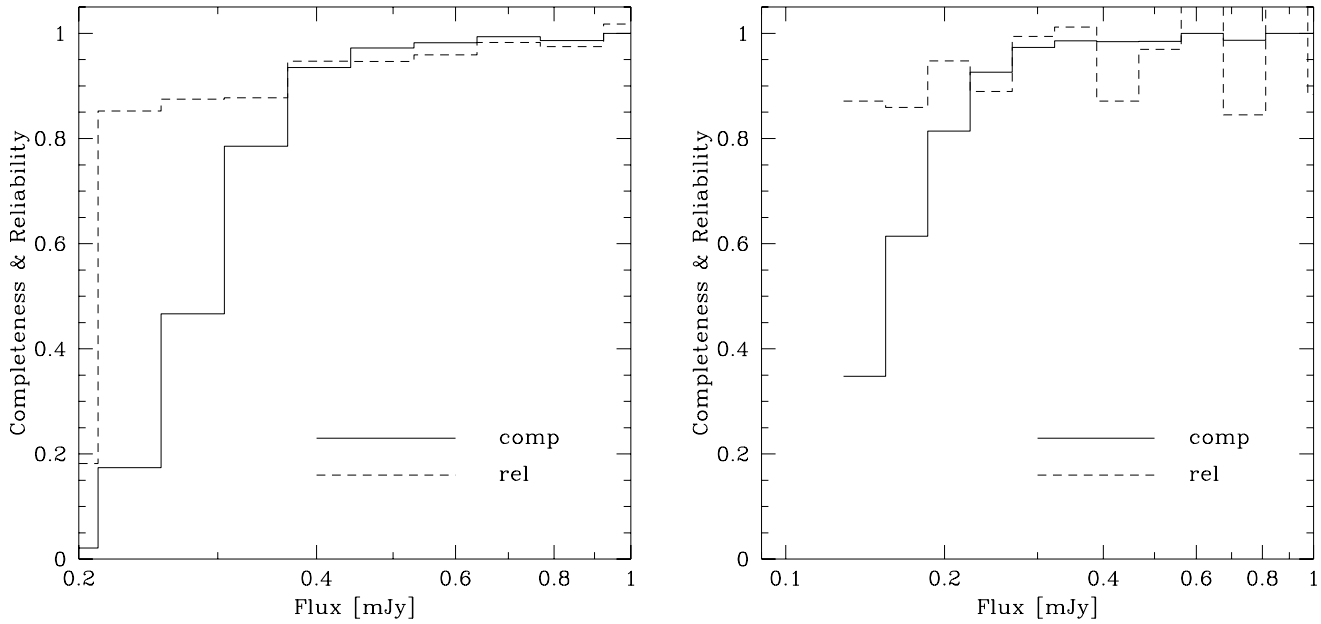


FIG. 13.—Completeness and reliability of the extracted sources at the 5 $\sigma$ level in the main (*left*) and verification (*right*) regions. According to our simulations, sources brighter than 0.21 and 0.12 mJy are highly reliable, and the surveys are 50% complete at 0.3 and 0.15 mJy in the main and verification regions, respectively.

sources is dominated by the astrometric error of the IR sources. We can obtain a formula to compute the astrometric error as a function of the S/N:

$$\sigma^2 = \sigma_{\rm ext}^2 + \sigma_{\rm point}^2, \tag{2}$$

where the pointing error $\sigma_{\rm point} = 0\farcs3$ and the error due to the extraction $\sigma_{\rm ext}$ is estimated from our simulations:

$$\log(\sigma_{\rm ext}) = 0.74 - 1.06 \log({\rm S/N}). \tag{3}$$

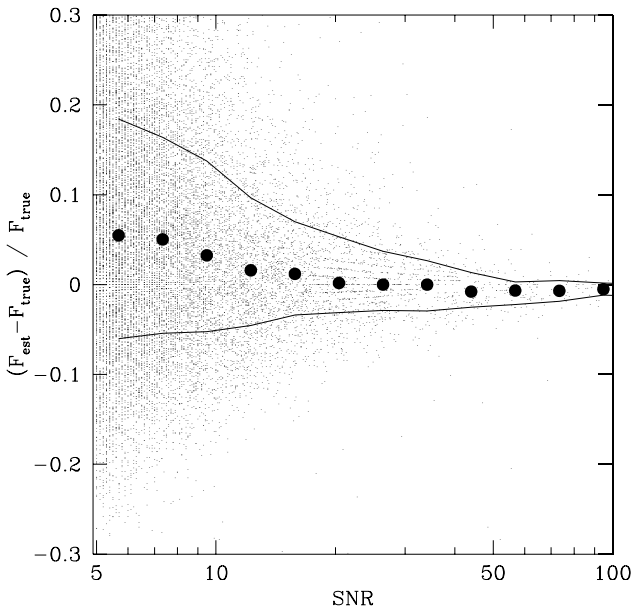


FIG. 14.—Difference between true and estimated fluxes vs. S/N for sources detected in the simulation. Points correspond to the sources. The large circles correspond to the median difference. The two lines mark the 1 $\sigma$ error band. The error increases toward low S/N values. Moreover, at low S/N values the estimated fluxes are biased toward higher values, since sources on positive fluctuations of the noise are preferentially detected.

### 4.5. *Aperture Correction*

Most of the sources detected in the FLS field at 24 $\mu$m are distant and, due to the low spatial resolution of the instrument, can be considered pointlike. Therefore, a good estimate of the total flux can be obtained by studying the aperture correction with a bright star.

A suitable bright star exists in the field. Because of its brightness, latencies are visible in the combined image. To eliminate the latencies from the mosaicked image, we subtracted from every BCD a fraction of the four BCDs taken before. We used for this task the empirical factors 0.007, 0.002, 0.002, and 0.001. The effect of the correction can be seen in Figure 17.

For comparison, a synthetic star has been obtained using the same BCDs around the real star with a theoretical PSF made with STinyTim (SED of a blackbody at 6000 K). This image has been mosaicked using the same reference frame as the real image, as well as masking the same pixels as in the real case.

After subtracting any point sources detected around the star, we subtracted an average value of 0.007 MJy sr$^{-1}$, which comes from residual background due to contribution of faint sources and has been estimated in regions close to the star. We then computed the flux in circular annuli around the real and synthetic stars. The azimuthally averaged profile is well reproduced by the model in the region including the first Airy ring (Fig. 18). Then, the real star appears slightly brighter than the synthetic one between 20″ and 50″, probably because of the contribution of a few faint sources that lie on the Airy rings and we were not able to detect and subtract.

For the radius that we are using in our extraction (11 pixels corresponding to 14.″02) the correction is 1.160 with the synthetic star and 1.169 with the real one. In Table 3 we report the aperture corrections computed for several apertures with the synthetic and real stars. The maximal aperture we considered in our measurements contained 99.45% of the total flux of the synthetic star. In our computation we assumed the same value also in the case of the real star.

We chose to use the theoretical factor (1.160) since the agreement with the real case is very good for radii less than 30″. The

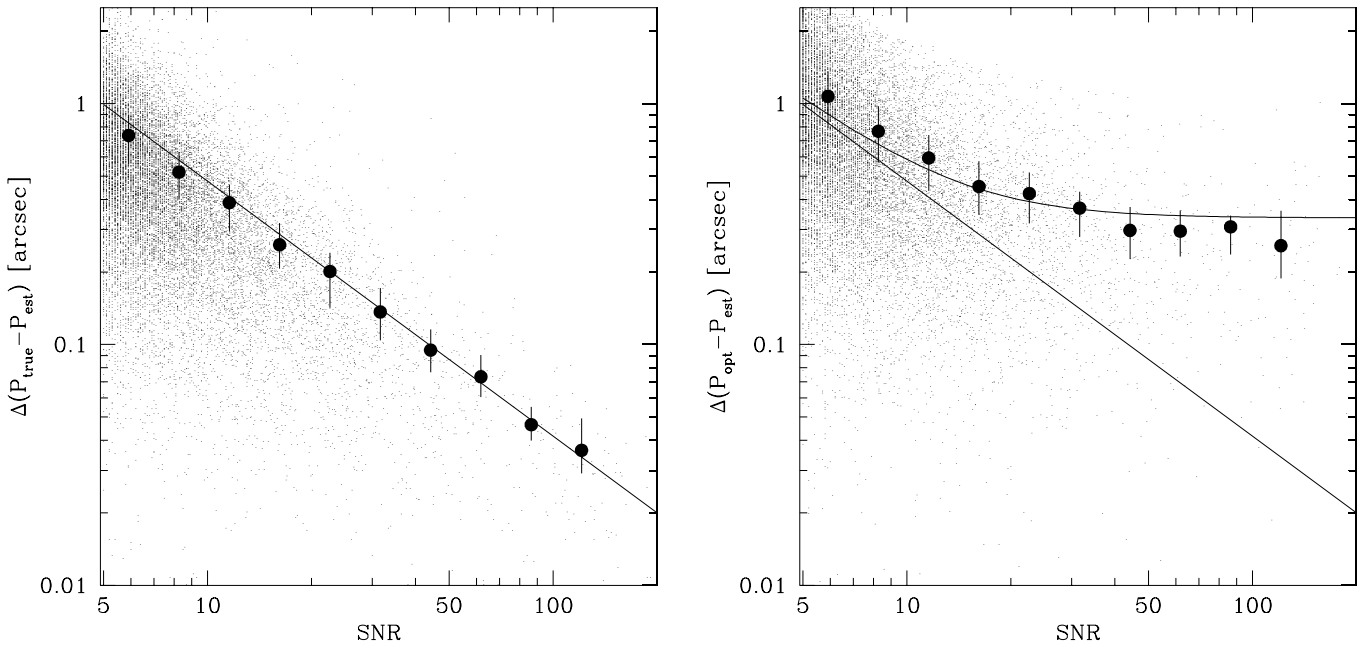


FIG. 15.—*Left:* Distance between true and estimated positions vs. S/N for simulated sources. Points correspond to the sources. The large circles correspond to the 1 $\sigma$ error (the distance within which one finds 68% of the counterparts). The error bars mark the 50th and 80th percentiles of the distribution of points. The line shows how the error depends on the S/N value. *Right:* Distance between IR sources and their optical counterparts. The 1 $\sigma$ error can be fitted by summing in quadrature the error computed from simulations (*straight line*) with the pointing error (0.″3) and the optical error (0.″1).

difference is less than 0.8%, and part of it probably comes from contamination of faint sources that we are not able to subtract. To overcome this limitation, one needs to stack several bright stars, which can be found when reducing many wide-field observations as, for instance, those in the SWIRE fields (Lonsdale et al. 2003).

We remind that, in the case of source extraction, we were able to follow such a procedure. In fact, since in this case we consider only the part inside the first Airy ring, we were able to build an empirical PRF stacking several bright isolated sources to obtain a PRF free of contamination by surrounding faint sources.

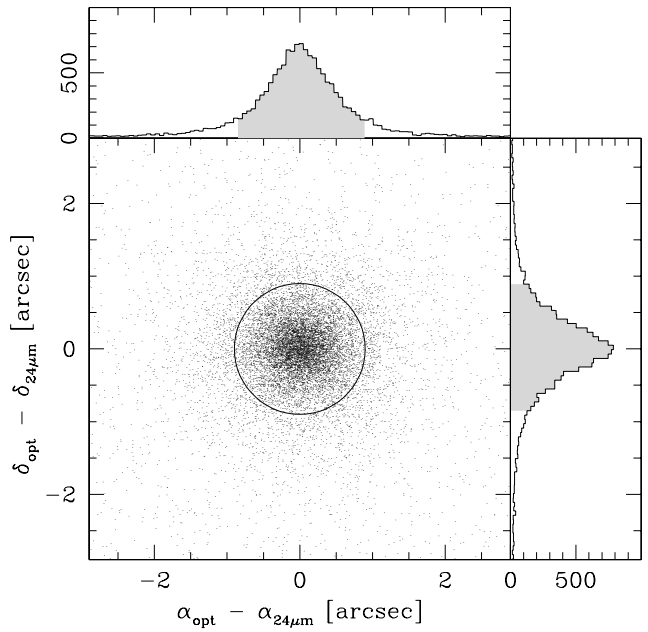


FIG. 16.—Differences in position between the IR sources and their optical counterparts; 68% of the counterparts are within a 0.″9 radius circle (see also shaded regions in the histograms).

### 4.6. *Absolute Calibration*

*Spitzer* calibration is based on routine observations of stars during every MIPS campaign and a set of stars with 24 $\mu$m fluxes between 0.02 and 2 Jy, observed one or more times since the commencement of MIPS observations. Based on the routine star observations, the calibration is stable from campaign to campaign within approximately 3%. The uncertainty of the flux conversion factor (0.04391 MJy sr$^{-1}$ DN$^{-1}$) is less than 5%, according to the MIPS Data Handbook.[5]

There are many reasons to check the calibration factor. Calibration stars were observed in photometry mode, and the FLS field was observed with medium-scan mode. The scan mode, which compensates for the motion of the telescope with the movement of the CSM, produces slightly broader PSFs than the photometric mode. Moreover, the technique used to reduce the calibration data is not identical to that used in this paper. Finally, although the calibration is remarkably stable, every campaign has a slightly different calibration factor.

To evaluate the importance of these effects, we used a set of 279 stars in the FLS field that have Sloan (in the five Sloan bands), 2MASS (in $J$, $H$, and $K_s$), and IRAC counterparts (at 3.5, 4.5, and 5.8 $\mu$m) within 2″. The main advantage of the FLS field for calibration purposes is that the Galactic extinction is very low [$E(B-V) \sim 0.022$ mag]. Although the extinction is generally lower for most of the stars, we applied a general correction to the visible and near-IR fluxes using the Galactic extinction. Optical, near-IR, and IR fluxes are used to fit star SEDs with a grid of Basel2.2 models (Lejeune et al. 1998). We do not use the 8 $\mu$m IRAC fluxes for the fit since the models do not take into account the SiO absorption feature at this wavelength. On the basis of the SED fits, we discarded from the original sample 13 probable AGNs and 35 stars with IR excess in the *IRAS* and MIPS bands. We considered only stars with predicted flux greater than 0.2 mJy for computing the calibration factor since for fainter stars the

[5] See http://ssc.spitzer.caltech.edu/mips/dh.

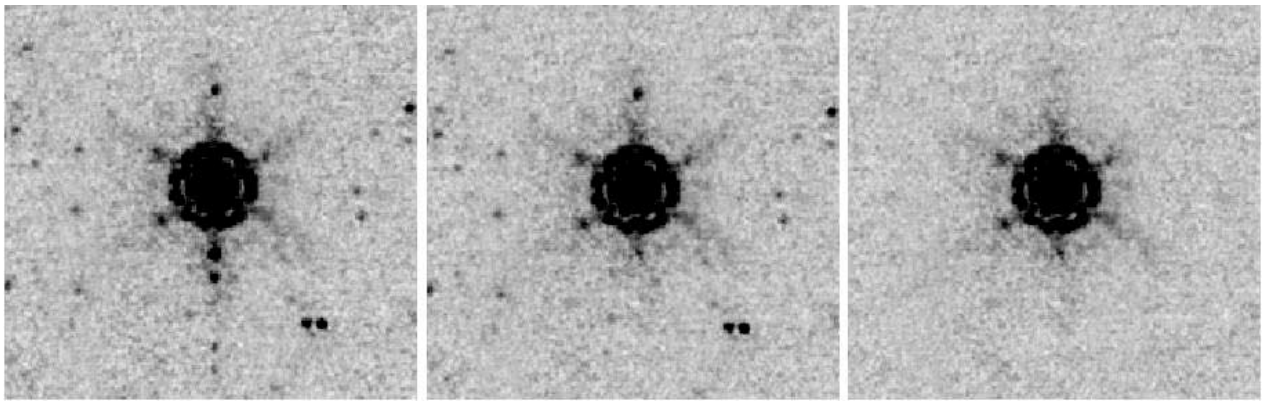

FIG. 17.—Image before (*left*) and after (*middle*) the latency correction and after the subtraction of surrounding sources (*right*). Four ghost sources below the star are visible in the image on the left. The field shown ($4\farcm7 \times 4\farcm45$) roughly corresponds to that used in the study of the PSF profile.

photometry is not reliable enough. Furthermore, we discarded from the sample a few stars with IR excess at 24 $\mu$m (Fig. 19, *open circles*). On the basis of the 224 stars considered, the flux conversion factor is $0.0441\% \pm 0.0004\%$, less than 0.5% higher than that reported in the MIPS Data Handbook. To compute this value we fitted a line passing through the origin taking into account the errors of the two variables (see Fig. 19). To do this, we minimized the $\chi^2$, defined as

$$\chi^2 = \sum_{i=1,N} \frac{(y_i - k x_i)^2}{\sigma_{y_i}^2 + k^2 \sigma_{x_i}^2}, \tag{4}$$

where $x_i$ and $y_i$ are the measured and predicted fluxes, respectively, and $\sigma_{x_i}$ and $\sigma_{y_i}$ are the respective errors (see inset in Fig. 19 and Press et al. [1992] for the $\chi^2$ formula). The data used for the fits, as well as predicted fluxes at 24 $\mu$m and the features of the best-fit SEDs, are reported in Table 4 (the entire list is available in the electronic edition of the *Astronomical Journal*). Since the *Spitzer* calibration is done with well-known stars and our value is well inside the error bar of the official calibration, we retained the official flux conversion value for computing the fluxes in our catalogs.

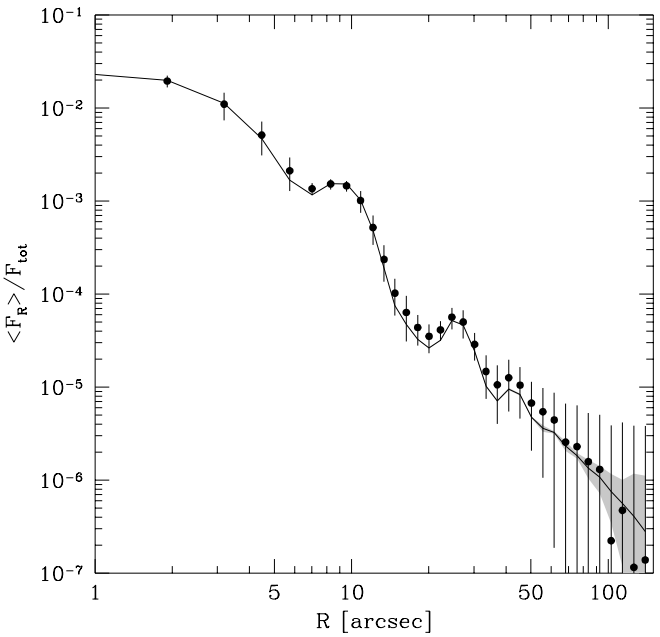


FIG. 18.—Azimuthally averaged profile normalized to the total flux of the source. The line and circles correspond to the synthetic and real sources, respectively. The first three Airy rings are clearly visible. Error bars correspond to the 1 $\sigma$ dispersion of fluxes inside the annulus. The shaded region corresponds to the same 1 $\sigma$ dispersion for the synthetic star.

### 4.7. *Color Correction*

*Spitzer* 24 $\mu$m calibrations are done with stars, and the official calibration is referred to a blackbody with an effective temperature of 10,000 K (see MIPS Data Handbook). When observing extragalactic objects, the slope of their SEDs is expected to be different from those of stars. According to the MIPS Data Handbook, the color correction is:

$$K = \frac{\int \left(F_\lambda F_{\lambda_0}^{-1}\right) \lambda R_\lambda \, d\lambda}{\int (\lambda_0/\lambda)^5 \left(e^{hc(\lambda_0 kT_0)^{-1}} - 1\right) \left(e^{hc(\lambda kT_0)^{-1}} - 1\right)^{-1} \lambda R_\lambda \, d\lambda}, \tag{5}$$

where $\lambda_0 = 23.675$ $\mu$m is the effective wavelength of the MIPS 24 $\mu$m band, $T_0 = 10,000$ K, and $R_\lambda$ is the response function. In Figure 20 we have computed this term in the case of three template galaxies in the range of redshift 0–2.5. The color term is very close to 1 at least up to $z = 1.1$. At higher redshifts, the PAH emission and Si absorption features fall into the filter, and huge variations are expected, especially in the case of starburst galaxies. Since there is no systematic correction independent of the

TABLE 3
APERTURE CORRECTIONS

| Radius (arcsec) | Theoretical Correction | Percent | Empirical Correction | Percent |
|---|---|---|---|---|
| 5.10..... | 1.912 | 52.3 | 1.986 | 50.4 |
| 6.38..... | 1.723 | 58.1 | 1.773 | 56.4 |
| 7.65..... | 1.590 | 62.9 | 1.610 | 62.1 |
| 8.93..... | 1.467 | 68.2 | 1.481 | 67.5 |
| 10.20..... | 1.323 | 75.6 | 1.339 | 74.7 |
| 11.47..... | 1.224 | 81.7 | 1.241 | 80.6 |
| 12.75..... | 1.182 | 84.6 | 1.194 | 83.8 |
| 14.02..... | 1.160 | 86.2 | 1.169 | 85.5 |
| 15.30..... | 1.153 | 86.7 | 1.158 | 86.3 |
| 16.57..... | 1.147 | 87.2 | 1.150 | 86.9 |
| 17.85..... | 1.142 | 87.6 | 1.144 | 87.4 |
| 19.12..... | 1.139 | 87.8 | 1.139 | 87.8 |

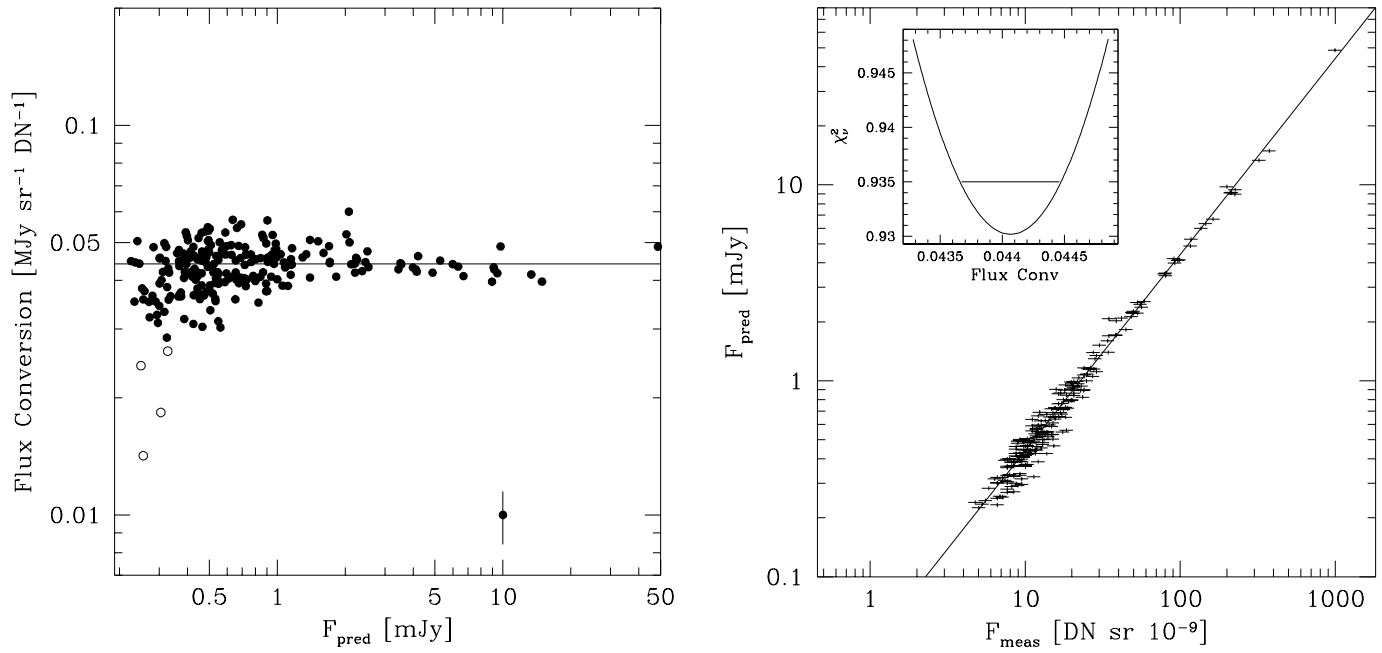


FIG. 19.—*Left:* Calibration factor vs. predicted flux for 24 $\mu$m stars in the FLS with SDSS, 2MASS, and IRAC counterparts. The point in the bottom right corner indicates the typical error bar. The open circles are stars with possible excess of IR emission not considered in our analysis. *Right:* Relationship between predicted and measured values of the flux for the 224 stars marked with filled circles in the left panel. The value found is less than 0.5% higher than the official 24 $\mu$m *Spitzer* calibration value (see horizontal line in the left panel). One sigma error bars are reported on the plots. The inset shows the reduced $\chi^2$ as a function of the calibration value. The horizontal line corresponds to the 1 $\sigma$ confidence interval.

redshift, we did not apply any color correction to the value of the fluxes measured in our catalog.

## 5. CIRRUS FOREGROUND

The careful method used to subtract zodiacal light and transient effects allowed us to study the foreground variations at 24 $\mu$m due to molecular cloud emission. In order to get rid of source emissions, we subtracted the point sources extracted at the 3 $\sigma$ level from the final mosaic image using the PRF estimated from the data and the fluxes computed with MOPEX. For the extended sources, it is not possible to perform such a subtraction. Therefore, we masked the regions containing the extended sources and substituted them with interpolated values. The residual image and the list of pixels masked are part of the data released with the paper (see § 7). To enhance the structures present in the residual image, we degraded the resolution of the original image to a pixel scale of 19″. The value of a pixel corresponds to the average of $15 \times 15$ pixels in the original image, which greatly reduces the noise.

Several structures are clearly visible in Figure 21. When compared to the neutral hydrogen emission maps of Lockman & Condon (2005), the main structures correspond to low-velocity

TABLE 4
STARS USED FOR ABSOLUTE CALIBRATION

| R.A. (J2000.0) | Decl. (J2000.0) | SDSS $u'$ | SDSS $g'$ | SDSS $r'$ | SDSS $i'$ | SDSS $z'$ | 2MASS $J$ | 2MASS $H$ | 2MASS $K_s$ |
|---|---|---|---|---|---|---|---|---|---|
| 17 09 58.292 | +58 38 56.00 | 15.84 ± 0.06 | 14.93 ± 0.05* | 14.89 ± 0.04* | 12.42 ± 0.02 | 13.00 ± 0.02* | 11.10 ± 0.03 | 10.55 ± 0.03 | 10.45 ± 0.02 |
| 17 10 31.493 | +59 26 03.72 | 14.75 ± 0.06 | 11.37 ± 0.04 | 10.88 ± 0.03 | 10.74 ± 0.02 | 12.96 ± 0.03* | 9.81 ± 0.03 | 9.51 ± 0.03 | 9.45 ± 0.02 |
| 17 11 11.095 | +59 50 56.45 | 15.74 ± 0.06 | 15.23 ± 0.05* | 12.81 ± 0.03 | 12.53 ± 0.02 | 12.99 ± 0.02* | 11.30 ± 0.03 | 10.83 ± 0.03 | 10.73 ± 0.02 |
| 17 11 18.604 | +59 59 31.04 | 16.11 ± 0.06 | 15.16 ± 0.05* | 12.87 ± 0.03 | 14.63 ± 0.04* | 12.99 ± 0.02* | 11.11 ± 0.03 | 10.47 ± 0.03 | 10.32 ± 0.02 |
| 17 10 51.481 | +58 46 07.97 | 15.23 ± 0.06 | 16.26 ± 0.07* | 10.01 ± 0.03 | 12.70 ± 0.03* | 9.99 ± 0.02* | 8.36 ± 0.03 | 7.81 ± 0.03 | 7.67 ± 0.02 |

| R.A. (J2000.0) | Decl. (J2000.0) | IRAC 3.5 $\mu$m | IRAC 4.5 $\mu$m | IRAC 5.8 $\mu$m | $F24$ Measured | $F24$ Predicted | $T_{\rm eff}$ (K) | [Fe/H]$_\odot$ | log $g$ (cm$^{-2}$) |
|---|---|---|---|---|---|---|---|---|---|
| 17 09 58.292 | +58 38 56.00 | 19.4 ± 1.9 | 11.5 ± 1.1 | 7.3 ± 0.7 | 0.65 ± 0.07 | 0.53 ± 0.0 | 4500 | 1.50 | −1.50 |
| 17 10 31.493 | +59 26 03.72 | 48.5 ± 4.8 | 31.1 ± 3.1 | 18.4 ± 1.8 | 1.26 ± 0.13 | 1.34 ± 0.0 | 5250 | 0.00 | 1.00 |
| 17 11 11.095 | +59 50 56.45 | 15.0 ± 1.5 | 8.8 ± 0.9 | 5.4 ± 0.5 | 0.42 ± 0.04 | 0.40 ± 0.0 | 4750 | 1.00 | −1.00 |
| 17 11 18.604 | +59 59 31.04 | 20.5 ± 2.0 | 12.8 ± 1.3 | 8.7 ± 0.9 | 0.48 ± 0.05 | 0.63 ± 0.0 | 4250 | 4.50 | −1.50 |
| 17 10 51.481 | +58 46 07.97 | 164.2 ± 16.4 | 122.9 ± 12.3 | 93.1 ± 9.3 | 6.40 ± 0.64 | 6.33 ± 0.2 | 4500 | 1.00 | 1.00 |

NOTES.—Units of right ascension are hours, minutes, and seconds, and units of declination are degrees, arcminutes, and arcseconds. An asterisk indicates that the point was considered deviant in the fit. Table 4 is published in its entirety in the electronic edition of the *Astronomical Journal*. A portion is shown here for guidance regarding its form and content.

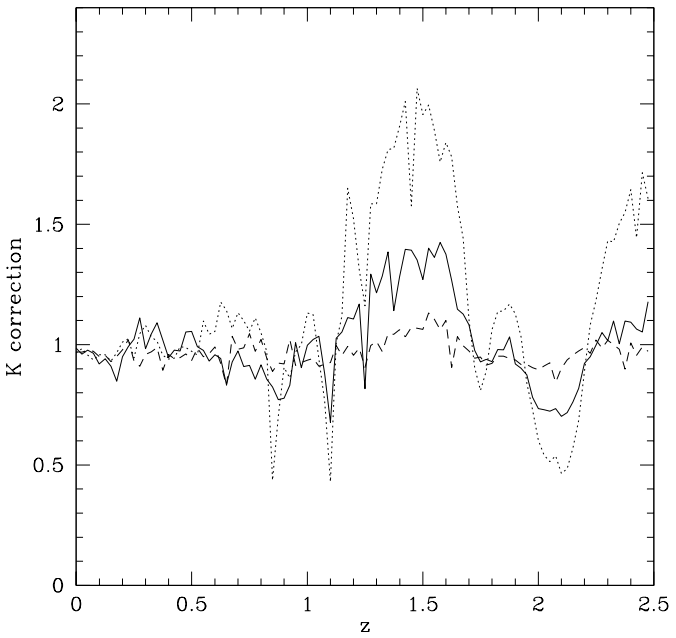


FIG. 20.—Color correction as function of the redshift for three different template galaxies: the starburst M82 (*dotted line*) and the Seyfert galaxies NGC 1068 (*dashed line*) and Circinus (*solid line*). Color correction is expected to be relevant only for sources beyond $z = 1.1$.

clouds. In particular, the arc is a cloud with velocity $V_{\rm LSR} = -2$ km s$^{-1}$. Also, a few intermediate-velocity structures are visible. The main ones are classified under the names IVC1 and IVC2 by Lockman & Condon (2005) and have velocities $V_{\rm LSR} = -41$ km s$^{-1}$.

## 6. RADIO AND OPTICAL ASSOCIATIONS

We searched for 24 $\mu$m source counterparts in the VLA 20 cm and in the KPNO *R* FLS catalogs (see Condon et al. 2003; Fadda et al. 2004a). The source density of the radio catalog is less than half that of the 24 $\mu$m sources (0.44 and 0.14 in the case of the main and verification fields, respectively). Therefore, it is rare to have two or more possible counterparts for a 24 $\mu$m source. Assuming a Poissonian distribution for the VLA sources, the probability of having more than one counterpart within a radius of 4″ is 0.4%. This is obviously not the case for the optical catalog, which contains almost 34 times the number of sources as the 24 $\mu$m catalog. In this case we have used a probabilistic approach to evaluate the reliability of the associations with 24 $\mu$m point sources. Associations of extended sources were treated separately by visually associating IR sources with radio and optical counterparts. The fluxes and magnitudes of the counterparts are reported in the detection Table 2.

### 6.1. *Radio Counterparts*

A fraction of 82% of the 24 $\mu$m field has been surveyed at 20 cm with the VLA (Condon et al. 2003) reaching a limiting flux of 0.1 mJy (see Fig. 1). We performed a cross-correlation between our 24 $\mu$m point-source catalog and the VLA catalog. For this comparison, we used a catalog of VLA sources that is slightly deeper than the 2003 version; 4904 VLA sources lie in our field. We found 2415 reliable associations with a positional difference of less than 4″, which roughly corresponds to 3 times the combined error of radio and 24 $\mu$m detections. This means that approximately 16% of our sample of 24 $\mu$m sources have 20 cm counterparts. There are no ambiguities in these associations, i.e., there is a unique counterpart found inside the chosen radius. In three cases the 24 $\mu$m point sources have extended radio sources as counterparts. We matched in the same way the extended source catalog, finding counterparts for 53% of the 94 sources inside the VLA field. The radio-IR associations are given in the point-source catalog (see § 7). For each associated radio source, we report its position, the 20 cm flux and the distance between the radio and 24 $\mu$m positions.

A fraction of 82% of the radio associations also have a reliable optical counterpart. This ratio is very similar to that of the IR sources with optical counterparts (see § 6.2), and therefore, it is essentially limited by the depth of the optical catalog used.

### 6.2. *Optical Counterparts*

The optical catalog we used for matching 24 $\mu$m sources is derived from the *R*-band KPNO observations of Fadda et al. (2004a). Since objects brighter than $R = 18$ are typically saturated in the KPNO data, we used the Sloan observations (D. W. Hogg et al. 2006, in preparation) to complete the bright magnitude range. To transform Sloan magnitudes into *R* magnitudes, we used the formula derived by Fadda et al. (2004a) through

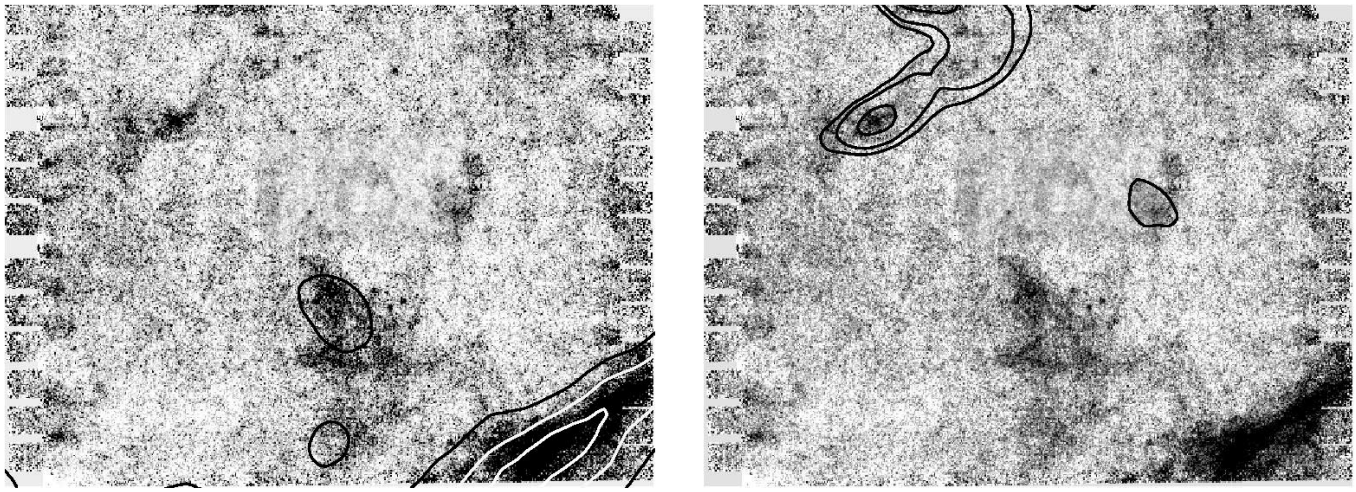

FIG. 21.—Cirrus foreground at 24 $\mu$m compared with the H I maps of Lockman & Condon (2005). North is up and east is left. *Left:* Low-velocity clouds ($-4.7$ km s$^{-1} < V < 0.7$ km s$^{-1}$) with $N_{\rm H\,I}$ contours corresponding to 0.16, 0.2, and $0.3 \times 10^{20}$ cm$^{-2}$. *Right:* Intermediate-velocity clouds ($-35$ km s$^{-1} < V < -45$ km s$^{-1}$) with $N_{\rm H\,I}$ contours corresponding to 0.87, 1.2, and $1.5 \times 10^{20}$ cm$^{-2}$.

calibration stars using the $r'$ and $i'$ magnitudes. The Sloan data homogeneously cover the entire 24 $\mu$m FLS field down to an $R$ magnitude of 23. The KPNO data cover most of the field with the exception of three corners (99.5% of the total area) with slightly variable depth. The typical limiting $R$ magnitude is 25.5. We considered only the part of the field covered by the KPNO data when searching for counterparts. To obtain a unique catalog from the various KPNO images, we first adjusted the astrometry of every image to that of the SDSS using SDSS counterparts of the KPNO sources. We then merged the catalogs of every image by completing them in the bright range with SDSS sources.

To compute the reliability of the optical associations we used the likelihood ratio technique described by Sutherland & Saunders (1992) following the Ciliegi et al. (2003) practical implementation. The likelihood ratio is defined as the ratio between the probability that an optical source is the real counterpart and the probability that the association is actually with a background object. Assuming that magnitudes and positions are not correlated, we can factorize the probability that a counterpart lies at a radius $r$ from the source and have a magnitude $m$:

$$p(r, m) = f(r)\, 2\pi r\, dr\, g(m)\, dm. \quad (6)$$

Therefore, the likelihood ratio is

$$L = \frac{f(r)g(m)}{b(m)}, \quad (7)$$

with $b$ the surface density of background objects at magnitude $m$. The reliability of an association with the $i$th candidate is defined as

$$R_i = \frac{L_i}{\sum_j L_j + (1 - G)}, \quad (8)$$

where the sum is done over the set of all possible candidates and $G$ is the probability that the candidate is brighter than the magnitude limit of the catalog [$G = \int^{m_{\rm lim}} g(m)\, dm$].

To estimate $g(m)$ we computed the overdensity of optical sources with respect to the background around each 24 $\mu$m source. In order to maximize the number of real counterparts we chose a radius approximately twice the 1 $\sigma$ error in position ($r_0 = 1\farcs6$). For each magnitude bin (0.5 mag between 16 and 25.5), we have an overdensity of possible counterparts with respect to the background of

$$o(m) = \sum_i N_{c,i} - N\, \pi r_0^2\, b(m), \quad (9)$$

where $N$ is the number of 24 $\mu$m point sources and $N_{c,i}$ is the number of possible counterparts for the source $i$ inside a circle of radius $r_0$ (see Fig. 22). To obtain the $g$-function, we normalize the overdensity and correct for the limiting magnitude of our catalog:

$$g(m) = \frac{o(m)}{\sum_i o(m_i)}\, G, \quad (10)$$

where $G$ is estimated on the basis of the ratio of the number of associations with the total number of 24 $\mu$m sources. We fixed $G = 0.8$, approximately the ratio of sources with optical counterparts. The number of counterparts, as well as their reliability, does not change substantially for $G$ in the range 0.7–0.9. As the probability function for the positional error we adopted a Gaussian distribution whose standard deviation takes into account the combination of IR and optical position accuracy.

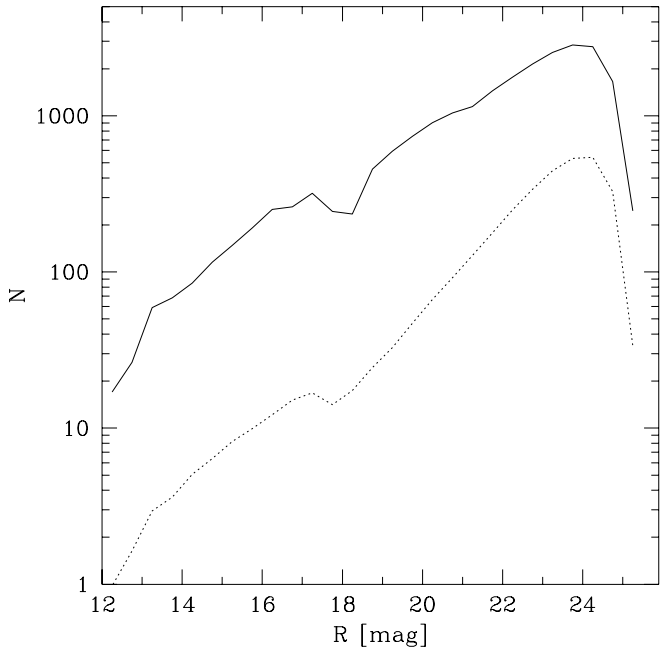


FIG. 22.—Magnitude distribution of possible counterparts (*solid curve*) and background objects (*dotted curve*) within a 2″ radius from each 24 $\mu$m source. The solid curve has been normalized according to eq. (10) and used in the likelihood ratio definition.

We searched for possible counterparts inside a circle of 5″ (approximately 5 $\sigma$ in radial position error) and accepted as possible counterparts the sources with likelihood ratio greater than $L_{\rm th} = 0.2$. With this threshold, the optical counterparts with only one identification (93% of the sample) and $L > L_{\rm th}$ have a reliability greater than 0.5. With this threshold we find that 13,783 out of the 16,823 sources detected at 24 $\mu$m within the area of the KPNO images have a likely identification, approximately 82%; 946 sources have more than one possible counterpart with $L > L_{\rm th}$, that is, 6% of the associations. In these cases, we assumed the object with the highest likelihood ratio value as the counterpart of the 24 $\mu$m source. The reliability of the association of sources with a unique counterpart is usually very high (0.9 in 92% of the cases).

The results of the optical identifications are reported in the point-source catalog (see § 7). For each 24 $\mu$m source we report the coordinates of the most probable optical counterpart within 5″, its $R$ magnitude, the distance between the IR and optical sources, and the reliability of the association.

## 7. DATA PRODUCTS

The images and catalogs produced in the analysis of the survey data are made available at the SSC science archive.[6]

### 7.1. *Images*

The images that are made publicly available are in FITS format and have a size of 171 Mbyte. The header contains the astrometric information and the tangential projection is used.

*Intensity map.*—Image with pixel size of 1.″275 and map units of MJy sr$^{-1}$. The image corresponds to the mosaic of the original BCDs reduced as explained in § 3.

[6] Using the Leopard archive tool or directly at http://data.spitzer.caltech.edu/popular/fls.

TABLE 5
FORMAT OF THE 24 $\mu$m POINT SOURCE CATALOG

| Column | Format | Description |
|---|---|---|
| 1–16 | a16 | IAU designation |
| 18–19 | i2 | R.A. hours (J2000.0) |
| 20–21 | i2 | R.A. minutes (J2000.0) |
| 22–27 | f6.3 | R.A. seconds (J2000.0) |
| 28 | a1 | Sign of declination |
| 29–30 | i2 | Decl. degrees (J2000.0) |
| 31–32 | i2 | Decl. minutes (J2000.0) |
| 33–37 | f5.2 | Decl. arcseconds (J2000.0) |
| 39–41 | f3.1 | Position error in arcseconds |
| 43–47 | f5.2 | 24 $\mu$m flux in mJy |
| 49–52 | f4.2 | 24 $\mu$m flux error in mJy |
| 54–58 | f5.1 | S/N of the detection |
| 60–61 | i2 | R.A. hours (J2000.0) of the optical counterpart |
| 62–63 | i2 | R.A. minutes (J2000.0) of the optical counterpart |
| 64–69 | f6.3 | R.A. seconds (J2000.0) of the optical counterpart |
| 70 | a1 | Sign of declination of the optical counterpart |
| 71–72 | i2 | Decl. degrees (J2000.0) of the optical counterpart |
| 73–74 | i2 | Decl. minutes (J2000.0) of the optical counterpart |
| 75–79 | f5.2 | Decl. arcseconds (J2000.0) of the optical counterpart |
| 81–85 | f5.2 | *R* magnitude of the optical counterpart |
| 87–89 | f3.1 | Distance between IR source and optical counterpart in arcsec |
| 91 | i1 | Number of possible optical counterparts within 5″ |
| 93–96 | f4.2 | Reliability of the most likely optical counterpart |
| 98 | i1 | Index of coverage (1 if out of KPNO field, 0 if inside the KPNO field) |
| 100–101 | i2 | R.A. hours (J2000.0) of the radio counterpart |
| 102–103 | i2 | R.A. minutes (J2000.0) of the radio counterpart |
| 104–109 | f6.3 | R.A. seconds (J2000.0) of the radio counterpart |
| 110 | a1 | Sign of declination of the radio counterpart |
| 111–112 | i2 | Decl. degrees (J2000.0) of the radio counterpart |
| 113–114 | i2 | Decl. minutes (J2000.0) of the radio counterpart |
| 115–119 | f5.2 | Decl. arcseconds (J2000.0) of the radio counterpart |
| 121–126 | f6.2 | 20 cm flux in mJy of the radio counterpart |
| 128–130 | f3.1 | Distance between IR source and radio counterpart in arcsec |
| 132 | i1 | Index of coverage (1 if out of VLA field, 0 if inside the VLA field) |

NOTE.—Table 5 describes the format of the data available in the electronic edition of the *Astronomical Journal*.

*Coverage map*.—Image with pixel size of 1.″275 and map units of number of BCDs. Since the integration time is 3.67 s per BCD, the exposure map can be obtained simply by multiplying this map by the exposure time per BCD.

*Uncertainty map*.—Map with a resolution of 1.″275 that has been used for the extraction of source positions. It has been computed with MOPEX assuming Poissonian noise plus a Gaussian component due to the readout noise with a dispersion of 40 $e^-$, mean of 0 $e^-$, and gain of 5 $e^-$ $DN^{-1}$.

*Residual map*.—Map with resolution of 1.″275 obtained by subtracting the point sources and masking and interpolating the regions occupied by extended sources.

*Bad pixel mask*.—Mask defining the regions occupied by extended sources that have been interpolated in the residual map. The file is given in the pixel-list IRAF format.

### 7.2. *Catalogs*

Three catalogs are given. The list of the 123 extended sources and their optical/radio counterparts (see Table 2) and the list of 231 stars considered for the calibration (Table 4) are offered in the complete form in the electronic edition of the *Astronomical Journal*.

The catalog of point sources including the optical and radio associations is an ASCII table with the format explained in Table 5 and is available in the electronic edition of the *Astronomical Journal*. The entries are ordered by decreasing S/N of 24 $\mu$m detections. The catalog contains 16,905 sources detected with a S/N > 5. The catalog reports the position errors and flux errors estimated from the simulations. The position error includes the effect of extraction and pointing errors. The flux errors do not account for the systematic error due to the calibration.

## 8. SUMMARY

A composite image of the 24 $\mu$m data in the First Look Survey region ($17^h18^m$, $+59°30'$) was obtained with SSC software packages and customized routines developed to further refine the reduction. In particular, self-calibration flats, illumination correction, and long-term transient correction were applied to the data to get rid of artificial variations of the background. A catalog of approximately 17,000 sources was extracted at the 5 $\sigma$ level using a PSF fitting technique (using the MOPEX package). The PSF was estimated from bright point sources in the field. For 123 extended sources detected in the field that cover less than 0.3% of the total area of the survey, aperture photometry was used. Aperture corrections and the absolute calibration are estimated using stars in the field. In particular, using a set of 224 stars with IRAC fluxes and optical and near-IR magnitudes we found an excellent agreement with the calibration factor used in the SSC pipeline. Completeness, reliability, and errors in astrometry and photometry are estimated through simulations. The 5 $\sigma$ cut of the

catalog guarantees high reliability of the extracted sources. The main and the verification surveys are 50% complete at 0.3 and 0.15 mJy, respectively. The astrometric and photometric errors are functions of the S/N of the source. Astrometric errors vary from 0.″3 up to 1.″1 for sources with decreasing S/N. Photometric errors (excluding the uncertainty in the calibration) reach 15% at the 5 $\sigma$ level and are approximately 5% for sources with S/N $\sim$ 20.

The 24 $\mu$m catalog has been cross-correlated with the KPNO $R$ and VLA 20 cm catalogs of the field (Fadda et al. 2004a; Condon et al. 2003). More than 80% of the 24 $\mu$m sources have a reliable counterpart down to the limiting depth of $R = 25.5$; 6% of these sources have multiple possible counterparts within 5″. Approximately 16% of the 24 $\mu$m sources have a 20 cm counterpart (down to 0.1 mJy), and $\sim$80% of these associations have a reliable optical counterpart.

Finally, by subtracting the detected point sources from the image down to the 3 $\sigma$ level and masking and interpolating the regions occupied by extended sources, we obtained a residual map that clearly shows the emission from extended Galactic cirri. By comparison with the H I data of Lockman & Condon (2005) we detect several clouds at low and intermediate velocities.

D. F. is grateful to Alberto Noriega-Crespo for enlightening discussions about MIPS data processing issues. We acknowledge also the anonymous referee for useful comments and suggestions.

REFERENCES

Appleton, P. N., et al. 2004, ApJS, 154, 147
Choi, P., et al. 2006, ApJ, 637, 227
Ciliegi, P., Zamorani, G., Hasinger, G., Lehmann, I., Szokoly, G., & Wilson, G. 2003, A&A, 398, 901
Condon, J. J., Cotton, W. D., Yin, Q. F., Shupe, D. L., Storrie-Lombardi, L. J., Helou, G., Soifer, B. T., & Werner, M. W. 2003, AJ, 125, 2411
Dickinson, M. 2001, BAAS, 33, 820
Elbaz, D., Cesarsky, C. J., Chanial, P., Aussel, H., Franceschini, A., Fadda, D., & Chary, R. R. 2002, A&A, 384, 848
Fadda, D., Jannuzi, B. T., Ford, A., & Storrie-Lombardi, L. J. 2004a, AJ, 128, 1
Fadda, D., et al. 2004b, A&A, 427, 23
Fazio, G. G., et al. 2004, ApJS, 154, 10
Frayer, D. T., et al. 2006, AJ, 131, 250
Gruppioni, C., Lari, C., Pozzi, F., Zamorani, G., Franceschini, A., Oliver, S., Rowan-Robinson, M., & Serjeant, S. 2002, MNRAS, 335, 831
Kelsall, T., et al. 1998, ApJ, 508, 44
Kessler, M. F., et al. 1996, A&A, 315, L27
Lacy, M., et al. 2005, ApJS, 161, 41
Lejeune, T., Cuisinier, F., & Buser, R. 1998, A&AS, 130, 65
Lockman, F. J., & Condon, J. J. 2005, AJ, 129, 1968
Lonsdale, C. J., et al. 2003, PASP, 115, 897
Makovoz, D., & Marleau, F. R. 2005, PASP, 117, 1113
Marleau, F. R., et al. 2003, BAAS, 203, 90.11
———. 2004, ApJS, 154, 66
Miville-Deschênes, M. A., Boulanger, F., Abergel, A., & Bernard, P. 2000, A&AS, 146, 519
Morganti, R., Garrett, M. A., Chapman, S., Baan, W., Helou, G., & Soifer, T. 2004, A&A, 424, 371
Press, W. H., Teukolsky, S. A., Vetterling, W. T., & Flannery, B. P. 1992, Numerical Recipes in C: The Art of Scientific Computing (Cambridge: Cambridge Univ. Press)
Rieke, G., et al. 2004, ApJS, 154, 25
Schlegel, D., Finkbeiner, D., & Davis, M. 1998, ApJ, 500, 525
Serjeant, S. B. G., et al. 1997, MNRAS, 289, 457
Shim, H., Im, M., Park, S., Choi, P., Fadda, D., Helou, G., & Storrie-Lombardi, L. 2006, ApJS, 162, 38
Soifer, B. T., Neugebauer, G., Beichman, C. A., Houck, J. R., & Rowan-Robinson, M. 1983, Proc. SPIE, 428, 297
Sutherland, W., & Saunders, W. 1992, MNRAS, 259, 413
Werner, M., et al. 2004, ApJS, 154, 1
Yan, L., et al. 2004, ApJS, 154, 60